Rare Metals

WILEY | 有科出版 YOUKE PUBLISHING

ORIGINAL ARTICLE OPEN ACCESS

Impact of Sb-Doping on the Reversible Li^+ and Na^+ Storage in CeO_2-Type Negative Electrodes

Yunjie Li[1,2] | Xilai Xue[1,2] | Seyed Javad Rezvani[3,4] | Giovanni Orazio Lepore[5] | Holger Euchner[6] | Angelo Giglia[4] | Thomas Diemant[1,2] | Yueliang Li[1,2,7] | Ute Kaiser[7] | Dariusz Mitoraj[8] | Radim Beranek[8] | Argjend Blakaj[1,2] | Alessandro Puri[9,10] | Francesco d'Acapito[9] | Vittorio Marangon[1,2] | Dominic Bresser[1,2,11]

[1]Helmholtz Institute Ulm (HIU), Ulm, Germany | [2]Karlsruhe Institute of Technology (KIT), Karlsruhe, Germany | [3]INFN, Laboratori Nazionali di Frascati, Frascati, Italy | [4]Laboratorio TASC, Consiglio Nazionale delle Ricerche (CNR), IOM-CNR, Trieste, Italy | [5]Department of Earth Sciences, University of Florence, Florence, Italy | [6]Institute of Physical and Theoretical Chemistry, University of Tübingen, Tübingen, Germany | [7]Central Facility for Materials Science Electron Microscopy, Ulm University (UUlm), Ulm, Germany | [8]Institute of Electrochemistry, Ulm University (UUlm), Ulm, Germany | [9]CNR-IOM-OGG c/o ESRF- The European Synchrotron, Grenoble, France | [10]Department of Physics and Astronomy, Alma Mater Studiorum—University of Bologna, Bologna, Italy | [11]Ulm University (UUlm), Ulm, Germany

Correspondence: Vittorio Marangon (vittorio.marangon@kit.edu) | Dominic Bresser (dominic.bresser@kit.edu)

Received: 8 December 2025 | **Revised:** 30 March 2026 | **Accepted:** 31 March 2026

Keywords: anode | insertion | lithium battery | Sb doping | sodium battery

ABSTRACT

Insertion-type metal oxide anode materials for lithium-ion and sodium-ion batteries commonly offer excellent cycling stability. However, their reversible capacity is eventually constrained by the finite number of available active sites within their crystal structures. Herein, the effect of introducing Sb into insertion-type CeO_2 (Sb-CeO_2) is investigated as an effective strategy to overcome this intrinsic limitation. Compared to neat CeO_2, it shows a substantially increased capacity owing to the extended redox activity of the Sb dopant while generally maintaining the insertion-type reaction mechanism of the CeO_2 host matrix. Interestingly, Sb-CeO_2 demonstrates promising performance in both Li-cells and Na-cells. Although the capacity contribution of Sb is slightly reduced in Na-cells compared to Li-cells, the former benefit from a highly stable solid electrolyte interphase layer and a remarkable rate capability in combination with an ether-based electrolyte. This is demonstrated also in sodium-ion cells comprising an Sb-CeO_2 anode and a $Na_3V_2(PO_4)_3$ cathode, showing excellent power performance up to a dis-/charge rate of 50C.

1 | Introduction

The extensive and continuously increasing global demand for efficient and sustainable energy storage technologies has rapidly accelerated the investigation and further development of advanced secondary batteries, particularly Li-ion and Na-ion batteries (LIBs, SIBs) [1, 2]. Although LIBs dominate mobile electronics and electric vehicles largely thanks to their high energy density and long-term cycling stability [3], concerns regarding lithium cost, resource abundance, and distribution have stimulated increasing interest in SIBs as a promising alternative, especially in the context of grid-scale energy storage applications [4–6]. For both technologies, the performance of the electrode materials, especially the anode material, remains critical for achieving a remarkable energy density, fast-charging capability, and long-term stability [7].

Carbon-based anodes, specifically, graphite and hard carbon, are currently the state of the art for commercial LIBs and SIBs, respectively, owing to their high capacity and good cycling stability in combination with relatively low cost [8–12]. However, their low de-/lithiation and de-/sodiation potentials increase the likelihood of metal plating, particularly when

applying high current densities and/or when operated at low temperatures, thereby raising safety concerns and limiting their fast-charging capability [13, 14].

A potential alternative is alloying-type anode materials such as Sb, Sn, or Si, which offer even higher theoretical capacities commonly, but suffer from severe volume changes during cycling, which results in an unstable solid electrolyte interphase (SEI), electrode pulverization, and rapid capacity fading [15–24]. Insertion-type metal oxides such as $Li_4Ti_5O_{12}$, TiO_2, and CeO_2 have therefore been explored as safer alternatives for LIBs and SIBs due to their relatively higher operating potentials, which effectively suppresses the risk of metal deposition compared with carbon-based anodes [12, 25–30]. In addition, their rigid oxide frameworks accommodate Li^+/Na^+ ions with minimal lattice distortion, resulting in reduced mechanical stress and excellent cycling stability [26–28]. However, their practical application is often constrained by relatively low reversible capacities, arising from the intrinsically limited redox activity of the comprised transition metal cations [25, 28, 30]. Overcoming this capacity limitation, while preserving the inherent safety and structural stability of insertion-type materials, remains a veritable challenge and has motivated the development of various strategies, including advanced material designs and compositional engineering [26, 28, 30, 31].

For our approach to complement these advances, we chose CeO_2 as a model electrode material because of its good structural stability as a robust host framework with cerium being able to be reversibly reduced from Ce^{4+} to Ce^{3+} and its three-dimensional oxygen sublattice in the fluorite structure that provides open pathways, enabling fast ion diffusion [28, 30]. Recent studies have demonstrated that introducing redox-active dopants can expand the charge-storage mechanism of CeO_2 beyond the classical insertion [28, 30]. For example, Fe-doped CeO_2 enables an additional redox reaction (Fe^{3+}/Fe^0), significantly enhancing capacity without compromising structural robustness [28]. A variety of dopants has been explored (outside the battery research domain) to tune the electronic structure and defect chemistry of CeO_2, including cations such as Zn^{2+}, Gd^{3+}, Nb^{5+}, and Sn^{4+} [32–35]. These dopants have been shown to change the oxygen-vacancy concentration and modify the electronic conductivity. However, it remains unclear whether potentially redox-active dopants—particularly those capable of a multi-electron conversion—can further extend this concept and enable higher capacities, while maintaining fast charge storage kinetics.

Herein, we investigate Sb-doped CeO_2 (Sb-CeO_2), serving as a new anode material for LIBs and SIBs to explore whether Sb can introduce an additional redox reaction within the CeO_2 host. A comprehensive set of electrochemical measurements combined with X-ray techniques, including operando X-ray diffraction (XRD), ex situ X-ray absorption spectroscopy (XAS), ex situ soft-XAS, and ex situ X-ray photoelectron spectroscopy (XPS), is utilized to elucidate the reaction process and surface chemistry. The Sb-CeO_2 electrode demonstrated promising performance within Li-cells and Na-cells, providing a remarkable rate capability, as also demonstrated in Sb-CeO_2‖$Na_3V_2(PO_4)_3$ (NVP) full-cells at dis-/charge rates up to 50C.

2 | Experimental

Synthesis: Sb-CeO_2 was synthesized using a hydrothermal reaction. In more detail, 3.908 g of $Ce(NO_3)_3{\cdot}6H_2O$ (Thermo Scientific) and 0.2281 g of $SbCl_3$ (Sigma-Aldrich) were dispersed into 60 mL of deionized water under continuous stirring for at least 1 h. Subsequently, 15 mL of an aqueous 5 mol L^{-1} NaOH (Sigma-Aldrich) solution was added dropwise to the mixture under constant magnetic stirring. The product was loaded into a 100-mL Teflon-lined vessel of a stainless-steel autoclave (Berghof BR-100) and subjected to hydrothermal treatment at 200°C for 24 h with continuous stirring. After naturally cooling to ambient temperature, the produced precipitate was collected by centrifugation, thoroughly washed with deionized water and ethanol, and then dried at 60°C for 12 h. Neat CeO_2 was prepared analogously without adding $SbCl_3$.

Physicochemical characterization: XRD was performed on a diffractometer (Bruker D8 Advance) using Cu Kα radiation (λ = 1.5418 Å) over a 2θ range of 20°–140°. XPS spectra were obtained with a spectrometer (PHI 5800 Multi Technique ESCA system, Physical Electronics) using monochromatic Al Kα radiation (300 W). XPS spectra calibration was conducted by setting the C 1s peak to 284.8 eV. Samples were transferred into the XPS load lock under an inert atmosphere to protect the surface from contamination. XAS experiments were performed at the LISA beamline (BM-08) of the European Synchrotron Radiation Facility (ESRF) in Grenoble, France [36]. The study examined the Sb K-edge (30,491.2 eV) and the Ce L_{III}-edge (5723.4 eV), employing a pair of Si (311) flat monochromator crystals, which provided an energy resolution of around 4×10^{-5} ($\Delta E/E$). Harmonic rejection at the Ce and Sb K-edge ($E_{cut\text{-}off} \approx 41$ keV) and the Ce L_{III}-edge ($E_{cut\text{-}off} \approx 16$ keV) was achieved using focusing mirrors coated with Pt and Si, respectively. Data were collected in transmission or fluorescence mode, depending on the absorber weight. For the XANES region, energy increments of 0.5 eV for the Ce L_{III}-edge and 1 eV for the Ce and Sb K-edges were used, respectively, whereas the post-edge EXAFS region was recorded using a constant k step width of 0.05 $Å^{-1}$. The extraction of the structural EXAFS signal ($k{\bullet}\chi(k)$) was carried out following an established procedure, including the pre-edge background removal [37], spline modeling of the bare atomic background, edge step normalization using a region far above the edge, and energy calibration using the software ATHENA [38]. Model atomic clusters, centered on the absorber atom, were obtained using ATOMS [39], starting from the models reported by Barret et al. [40] for Sb-Sb scattering paths and Jansen [41] for Sb-O scattering paths, and modified in order to get satisfactory fit results. A simple model was also implemented for Sb-Sb/Ce scattering paths by randomly substituting Sb for Ce in the cerianite structure and fixing distances according to the fit results [42]. The FEFF8 code was used to generate phase functions and theoretical amplitude [43]. The ARTEMIS software was employed to fit EXAFS spectra in the Fourier-transform (FT) space [38]. The data are available at the ESRF data portal [44]. Ex situ soft-XAS was carried out at the BEAR beamline of Elettra in Trieste, Italy [45]. The signal was normalized to the incident beam and the monitor signal. The photon energy was calibrated using the C K-edge at $\pi-\pi^*$ excitation. The samples were placed in the load lock and experimental

chamber under an inert Ar atmosphere to prevent air exposure. UV–Vis absorption measurements were carried out between 200 and 800 nm using a UV–Vis spectrophotometer (Shimadzu UV-2600). (High-resolution) Transmission electron microscopy ((HR)TEM), energy dispersive X-ray spectroscopy (EDX), and selected area electron diffraction (SAED) were performed employing a Thermo Scientific Talos F200i microscope with a 200-kV operating voltage. The elemental composition of the materials was additionally analyzed by inductively coupled plasma optical emission spectrometry (ICP-OES) using a Spectro Arcos FHS12 spectrometer from Spectro Analytical Instruments. For this purpose, the samples were dissolved in aqua regia using a microwave digestion system to ensure complete dissolution.

Electrode preparation: The electrode slurries were prepared by combining the active material (CeO_2 or Sb-CeO_2), conductive carbon (Super C65T, TIMCAL) and binder (sodium carboxymethyl cellulose, CMC, and Dow Wolff Cellulosics) in deionized water with a weight ratio of 75:20:5 by ball milling for 2 h. Dendritic copper foil (Schlenk, 99.9%) was used as the current collector. After being dried at room temperature, the electrode tapes were cut into 12-mm discs with an active material mass loading of about 1.5 mg cm^{-2}. For the operando XRD measurements, employing a self-designed cell setup [46], the electrode slurries were prepared analogously but cast on a beryllium (Be) disk. For the ex situ XAS analysis, the CeO_2 and Sb-CeO_2 electrodes were prepared by spreading the slurries on carbon paper (QuinTech). The NVP cathode slurry (the NVP powder was synthesized following a previous report) [47], comprising the active material, conductive carbon (Super C65T, TIMCAL), and polyvinylidene fluoride (PVdF 6020, Solvay) in a 75:20:5 weight ratio in *N*-methyl-2-pyrrolidone (NMP, Sigma-Aldrich), was cast on aluminum foil and then dried at 60°C. The active material mass loading of the NVP cathodes was about 2.0 mg cm^{-2}.

Electrochemical characterization: CR2032 coin-type cells (Hohsen and MTI) were used for the electrochemical characterization. Half-cells were constructed with the prepared CeO_2 or Sb-CeO_2 electrodes as working electrodes, lithium or sodium metal discs as counter/reference electrodes, and glass fiber sheets (GF/D, Whatman) as separators. For the full Na-ion cells, the assembly followed a similar procedure, except that the metal disc was replaced with an NVP cathode. The capacity ratio of the negative and positive electrodes (N/P) was about 1.1. All cells were assembled in a glove box (MBraun, $H_2O < 1$ ppm; $O_2 < 1$ ppm) filled with Ar. The electrolyte for the Li-cells was 1M $LiPF_6$ in ethylene carbonate/diethyl carbonate (EC/DEC, mixed in a 3:7 weight ratio, UBE), whereas 1M $NaPF_6$ in dimethoxyethane (DME, Sigma-Aldrich) was used as an electrolyte for the Na-cells and full Na-ion cells. Cyclic voltammetry (CV) measurements were carried out either at a constant sweep rate of 0.1 mV s^{-1} between 0.01 and 3.0 V or at increasing sweep rates in the same potential range. Galvanostatic cycling was conducted at 0.1 A g^{-1} or increasing dis-/charge rates from 0.01 to 3.0 V for both Li-cells and Na-cells. The preliminary evaluation of the NVP cathode was carried out in Na-cells via galvanostatic cycling between 2.5 and 4.2 V using either increasing dis-/charge rates or a constant C rate of 20C set after 10 activation cycles at 1C (1C = 120 mA g^{-1}). Full Na-ion cells were cycled within a voltage range from 0.1 to 3.7 V at 20C after 10 activation cycles at 1C (1C = 120 mA g^{-1}) or at increasing dis-/charge rates. Electrochemical impedance spectroscopy (EIS) was carried out in a frequency range from 200 to 0.01 kHz using a voltage amplitude of 10 mV. The obtained Nyquist plots were analyzed using a nonlinear least squares (NLLS) fitting method exploiting the Boukamp software [48, 49], and only fits with a χ^2 value below 10^{-3} were accepted. A VMP 3 potentiostat (BioLogic) was used to conduct CV and EIS measurements. A Maccor 4000 battery tester was used to conduct the galvanostatic measurements. All electrochemical tests were carried out at 20°C using thermostatic climatic chambers.

DFT calculations: To investigate the atomic structure of Sb-CeO_2, and in particular the local environment of Sb, density functional theory (DFT) calculations were performed, applying the VASP code [50, 51]. The generalized gradient approximation in the formulation of Perdew, Burke, and Ernzerhof was used to account for exchange and correlation [52]. A $2 \times 2 \times 2$ supercell of CeO_2, containing 96 atoms, was created and subsequently optimized with respect to atomic coordinates and cell volume, using an energy cut-off of 600 eV in combination with a $3 \times 3 \times 3$ k-point mesh. Furthermore, by replacing a Ce atom with Sb, a $Sb_{0.0625}Ce_{0.9375}O_2$ phase was created and optimized with the same settings. Subsequently, different positions of the Sb atom and distortions of the surrounding local environment were investigated.

3 | Results and Discussion

3.1 | Synthesis and Physicochemical Characterization

Sb-doped CeO_2 nanocrystals (Sb-CeO_2) were synthesized using a hydrothermal reaction. The XRD pattern with corresponding Rietveld refinement results is presented in Figure 1A. The observed Bragg reflections correspond to the *Fm*-3*m* space group with no detectable impurity phases such as Sb_2O_3 or Sb_2O_5 [53, 54], confirming the formation of a phase-pure material. The refined parameters for Sb-CeO_2 provided in Supporting Information S1: Table S1 indicate that the lattice parameter of the synthesized material, that is, $a = 5.4224(2)$ Å, aligns with that of cubic CeO_2, 5.4178(1) [28], although the incorporation of Sb seems to lead to a moderate lattice expansion, possibly arising from oxygen interstitials [55]. Compared with CeO_2, Sb-CeO_2 shows a significantly reduced Bragg reflection intensity, indicating a decreased order and crystallinity owing to the substitution of Ce by Sb (Supporting Information S1: Figure S1A). Raman spectra (Supporting Information S1: Figure S1B) show a sharp F_{2g} band near 465 cm^{-1} for CeO_2, corresponding to the M-O symmetric stretching in the fluorite lattice [56]. Sb incorporation caused a significant band broadening, indicative of an increased disorder—in line with the observations from the XRD results, whereas the absence of a feature near ~600 cm^{-1}, typically associated with oxygen vacancies [56, 57], suggests a negligible concentration of oxygen vacancies. The composition of the Sb-CeO_2 composite and the valence states of the constituent elements were first evaluated by XPS. The survey spectrum (Supporting Information S1: Figure S2A) shows the expected presence of cerium, oxygen, and antimony in the sample. The binding energies of the high-resolution peaks were referenced to the adventitious C 1s signal at 284.8 eV (Supporting Information

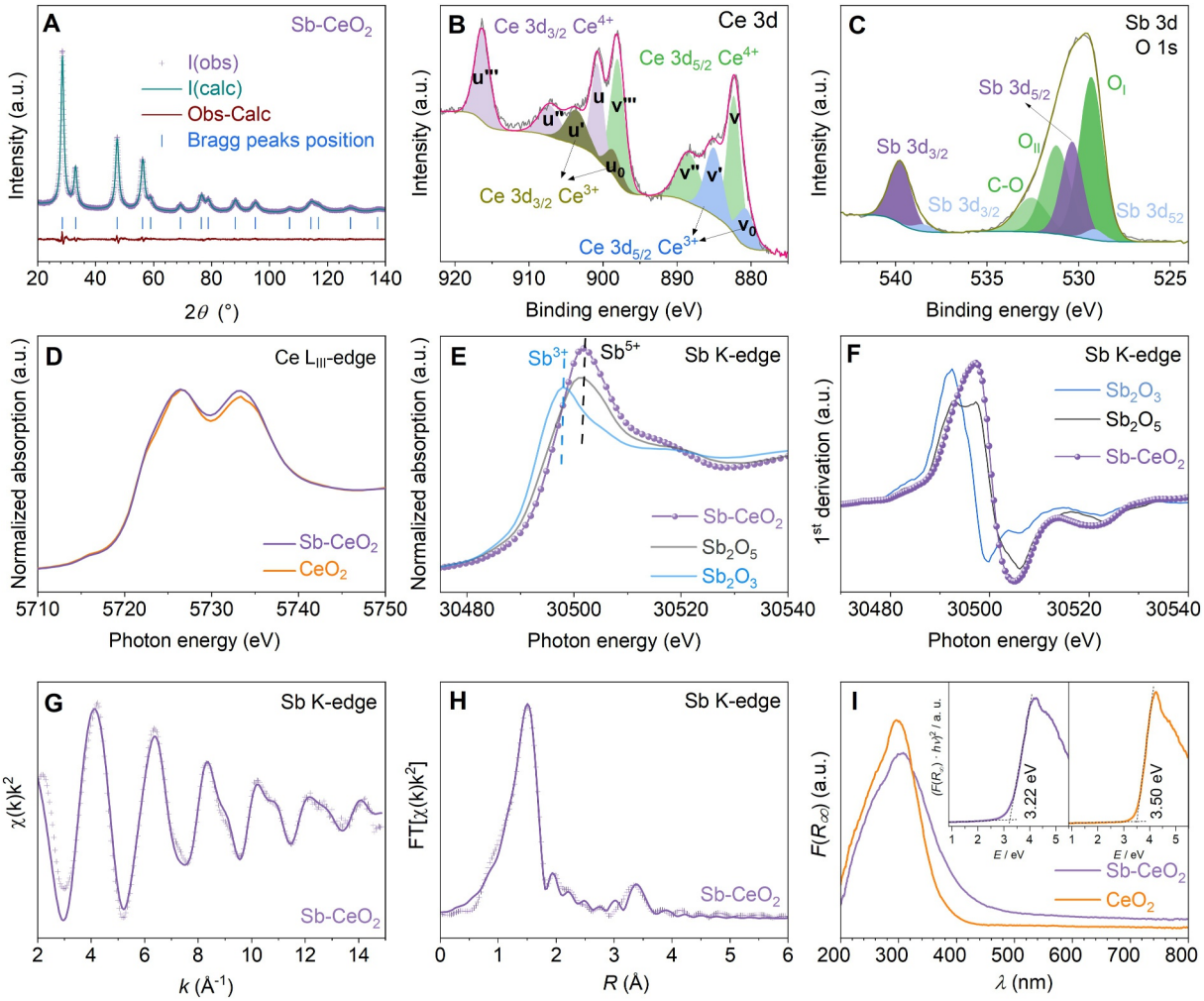

FIGURE 1 | Physicochemical characterization of the Sb-CeO_2 powder. (A) Rietveld refinement. High-resolution XPS spectra in the (B) Ce 3d and (C) Sb 3d/O 1s regions. (D) XANES spectra collected at the Ce L_{III}-edge for Sb-CeO_2 and CeO_2. (E) Sb K-edge XANES spectra and (F) the 1st derivative spectra of Sb-CeO_2 and of Sb_2O_3 and Sb_2O_5 reference compounds. (G) Sb K-edge k^2-weighted EXAFS region and (H) Fourier transform (uncorrected for phase shifts) of Sb-CeO_2 and relative multiparameter fit. (I) UV–Vis absorption spectra for Sb-CeO_2 and CeO_2. The insets show the corresponding Tauc plots for the energy band gap determination.

S1: Figure S2B). The Ce 3d high-resolution XPS spectra of CeO_2 (Supporting Information S1: Figure S3) and Sb-CeO_2 (Figure 1B) display multiple peaks arising from intrinsic multiplete splitting and final-state effects, characteristic of Ce 3d photoemission, and show the presence of both Ce^{4+} and Ce^{3+} species. For Sb-CeO_2, the peaks at binding energies of 882.3, 888.7, and 898.1 eV are assigned to Ce^{4+} (Ce $3d_{5/2}$), whereas those at 880.7 and 885.0 eV correspond to Ce^{3+} [58–60]. A finite Ce^{3+} contribution is also observed for CeO_2, which may be attributed to the partial reduction of Ce^{4+} under the ultrahigh vacuum conditions during the XPS measurement [57, 61]. Notably, the relative Ce^{3+} content is higher in Sb-CeO_2 than in CeO_2 (Supporting Information S1: Table S2), which may reflect a combined effect of measurement-induced surface reduction and Sb-induced modification of the local electronic structure and charge compensation. Since XPS is surface-sensitive, though, the bulk Ce oxidation state was further investigated using bulk-sensitive XAS, which will be discussed at a later stage. In the O 1s high-resolution spectrum shown in Figure 1C, the intense peak (O_I) at 529.4 eV is attributed to lattice oxygen [58, 60]. The second peak related to oxygen (O_{II}) at 531.2 eV is related to carboxyl/carbonate species, which are also seen in the C 1s spectra (Supporting Information S1: Figure S2B), and possibly also to hydroxyl groups [59]. Furthermore, it has been reported that oxygen anions near O vacancy sites in the vicinity of Ce^{3+} also contribute to this peak [58, 60, 62, 63]. Finally, the last oxygen peak at 532.6 eV corresponds to C-O groups. In addition to the oxygen peaks, a Sb 3d peak doublet at 530.3 and 539.7 eV is also detected. The measured binding energy is between that reported for Sb_2O_3 (~530 eV) and Sb_2O_5 (~531 eV) [64], whereas X-ray absorption near edge structure (XANES) analysis unequivocally demonstrates an extensive dominance of Sb^{5+} in Sb-CeO_2 (see below). The observed small downshift of the binding energy in Sb-CeO_2 compared to Sb_2O_5 is possibly related to a different environment for the Sb^{5+} cations [64]. Additional details on the chemical environment in Sb-CeO_2 are provided by the XANES analysis displayed in Figure 1D–F. The Ce L_{III}-edge spectra in Figure 1D, recorded for CeO_2 and Sb-CeO_2, exhibit nearly identical spectral profiles and edge positions with the characteristic double-peak feature of Ce^{4+}, and no obvious spectral signatures associated with Ce^{3+} are observed. This indicates that cerium remains predominantly in the Ce^{4+} state in

the bulk for both samples. Although XPS reveals a higher Ce^{3+} contribution at the surface for Sb-CeO_2, the XAS results suggest that such Ce^{3+} species are confined to the near-surface region or are below the detection limit of bulk-sensitive XAS. Moreover, the comparison of the normalized XANES spectra and relative first derivatives of Sb-CeO_2, Sb_2O_5, and Sb_2O_3 in Figure 1E,F indicates that the bulk oxidation state of Sb is Sb^{5+} in Sb-CeO_2. Based on the above results, it is concluded that Ce is predominantly present in the +4 oxidation state and Sb in the +5 state, with no clear experimental evidence for extensive oxygen or cation vacancies. Besides a potentially minor contribution from Ce^{3+} species in the near-surface region, charge neutrality may also be accommodated by the incorporation of interstitial oxygen [55], as suggested earlier by the observation of an expanded crystal lattice in the presence of Sb, and as further discussed in the following. Along these lines, the Sb K-edge EXAFS (Figure 1G,H, Supporting Information S1: Table S3) indicates that Sb^{5+} is locally coordinated by 6 O atoms at a distance of 1.97(1) Å, and the coordination number used for the fit is in perfect agreement with that derived using the bond-valence model (5.9) [65]. The analysis of the weak second shell peak centered at ~3.4 Å in the EXAFS Fourier transform (Figure 1H) can be fitted with a mixed Sb-Sb/Ce contribution, indicating that Sb is actually incorporated in the CeO_2 structure with a (very) minor tendency to cluster. The reduced apparent coordination number observed by EXAFS implies a local rearrangement of the oxygen sublattice around Sb. Such a rearrangement may involve the displacement of a subset of oxygen atoms to longer distances, rendering them less visible in the first coordination shell, and giving rise to an EXAFS-visible SbO_6 environment. Within this framework, charge compensation may be accommodated either by local lattice distortion, by the presence of a small amount of oxygen interstitials, or by a combination of both effects. The UV–Vis spectra of Sb-CeO_2 and CeO_2 in Figure 1I reveal a slight shift of the peak from 296 to 307 nm upon Sb doping, indicating a decrease of the band gap from 3.50 eV for CeO_2 to 3.22 eV for Sb-CeO_2, as depicted in the corresponding Tauc plots in the inset [66]. In addition to this band-gap narrowing, the substitution of Ce^{4+} by Sb^{5+} introduces extra electrons for charge compensation, which increases the electronic carrier concentration [67]. Together, these effects account for the enhanced electronic conductivity of Sb-CeO_2. In summary, the data presented in Figure 1 confirm that Sb has been successfully incorporated into the CeO_2 lattice, leading to an enhanced conductivity.

To better understand the crystal structure of Sb-CeO_2 and the possible local environments of Sb, DFT calculations were performed. Pristine CeO_2 adopts the cubic fluorite structure with Ce occupying the cation sites and forming a cubic on-center CeO_8 coordination (Figure 2A). Upon Sb substitution, Sb still preferentially occupies the Ce site in the fluorite lattice (Figure 2B, left). However, the local rearrangement of the surrounding oxygen sublattice can lead to distorted coordination environments in which Sb exhibits an effective sixfold coordination (SbO_6), with two additional oxygen atoms at longer distances (one representative model is shown in Figure 2B, right). Although the ideal on-center SbO_8 configuration is energetically slightly more stable, the energy difference relative to the distorted configurations is minimal, rather small (about 1 meV per atom). Taking into account that different orientations of the distorted configuration are possible, this will result in additional configurational entropy, such that for higher (preparation) temperatures and increasing Sb contents, the distorted configurations, featuring SbO_6 environments, may indeed become more stable.

The morphology and elemental distribution of/in Sb-CeO_2 were investigated by TEM-EDX, as displayed in Figure 2C–I. The analysis shows a primary particle size of less than 10 nm, as suggested by the low-magnification image in Figure 2C and confirmed by the high-resolution TEM micrograph shown in Figure 2D. The measured lattice fringes of 0.31 and 0.27 nm detected in Figure 2D can be assigned to the (111) and (200) planes of cubic CeO_2 [28], respectively, and are well matched by the selected area electron diffraction (SAED) rings presented in Figure 2E, which also shows the (220) and (311) planes of cubic CeO_2 [28], in agreement with the Rietveld refinement results discussed in Figure 1. Furthermore, the high-angle annular dark-field scanning TEM (HAADF-STEM) image in Figure 2F, combined with the EDX maps in Figure 2G–I, indicates that Sb is generally distributed rather homogeneously throughout the particles, whereas a few localized regions with relatively higher Sb intensity are observed as well. This distribution may be attributed to the low Sb doping level combined with differences in atomic number contrast and the limited spatial resolution and thickness sensitivity inherent to EDX analysis. Nonetheless, EXAFS fitting suggests a (very) minor Sb-Sb contribution, indicating that a small degree of local Sb clustering cannot be excluded. The atomic percentages of Ce and Sb were examined by both EDX and ICP-OES analyses (Supporting Information S1: Table S4). Although EDX provides semi-quantitative information and indicates a Ce/Sb atomic ratio close to 9/1, ICP-OES measurements are supposed to yield a more accurate Ce/Sb ratio, which also turns out to be around 9/1, thus confirming the EDX results and, as a result, the intended stoichiometry.

3.2 | Electrochemical Characterization

The electrochemical properties of Sb-CeO_2 were evaluated in Li and Na half-cells. The CV data for Sb-CeO_2 in Li-cells are presented in Supporting Information S1: Figure S4. The cathodic peaks observed during the first cycle at 1.27 and 0.60 V versus Li^+/Li are assigned to the partial decomposition of the electrolyte to form an SEI layer and to the Li^+ uptake within the Sb-CeO_2 matrix, respectively, accompanied by the reduction of Ce and Sb according to the Ce^{4+}/Ce^{3+} and Sb^{5+}/Sb^{3+} (or Sb^0) redox couples [68, 69], whereas the reduction peak at 0.01 V versus Li^+/Li suggests the Li insertion into the conductive carbon [70]. Accordingly, the following broad anodic peak at 0.25 V versus Li^+/Li is assigned to the deinsertion of Li^+ from the conductive carbon, and the broad peaks between 1.2 and 2.0 V versus Li^+/Li are assigned to the Li^+ extraction from Sb-CeO_2 and the re-oxidation of the redox-active elements [71]. During the following cycles, a shift of the Ce/Sb reduction potential to around 0.8 V versus Li^+/Li and the modification of the signal shape to a broad wave are observed, reflected during charge by the centering of the oxidation process at 1.2 V versus Li^+/Li. The decrease in polarization of the reduction and oxidation processes, accompanied by an increase in the current intensity for both processes, indicates the enhanced kinetics and efficiency of the redox processes of Ce and Sb [70]. The galvanostatic dis-/charge profiles

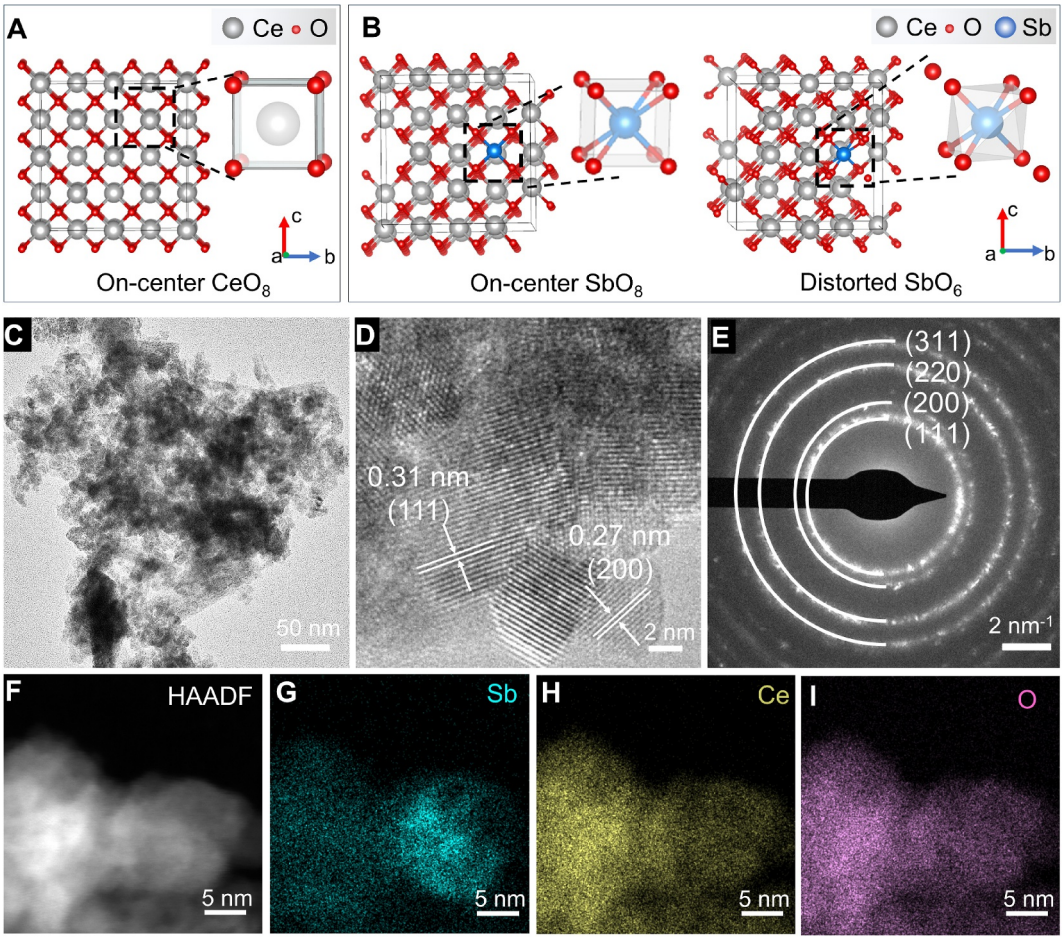

FIGURE 2 | Structural characterization of Sb-CeO_2. (A) Crystal structure of pristine CeO_2 with the fluorite lattice and (B) optimized crystal structure of Sb-doped CeO_2 obtained from DFT calculations. (C) Overview TEM and (D) HR-TEM micrographs. (E) SAED pattern. (F) HAADF-STEM micrograph, and the corresponding EDX elemental mapping results of (G) Sb, (H) Ce, and (I) O.

reported in Figure 3A related to the long-term cycling of Li‖Sb-CeO_2 cells at 0.1 A g^{-1} show an initial discharge and charge capacity of 235 and 153 mAh g^{-1}, respectively, resulting in a first-cycle Coulombic efficiency (CE) of 65%, accounting for a relatively high irreversible capacity caused by SEI formation. In accordance with the CV data, the following cycles exhibit a gradual shape change of the voltage profiles with a shift to lower potentials. The improvement in efficiency of the Sb-CeO_2 electrochemical process in Li-cells is well displayed in Figure 3B. Indeed, the CE shows a gradual increase from 65% to 95% in the first 7 cycles, eventually stabilizing at 99%, whereas the charge capacity reaches a maximum of 153 mAh g^{-1} within the initial 7 cycles and stabilizes at 122 mAh g^{-1} at the 150th cycle, resulting in a capacity retention of 80%. Differently, the CeO_2 reference electrode shows an initial discharge and charge capacity of 199 and 136 mAh g^{-1}, respectively. The charge capacity decreases in the following and arrives at 89 mAh g^{-1} after 100 cycles, yielding to a retention of only 65%, as depicted in Supporting Information S1: Figure S5. The increased specific capacity and capacity retention of Sb-CeO_2 stems from the incorporation of Sb into the CeO_2 lattice. The rate capability of Sb-CeO_2 in Li-cells was also investigated, showing charge capacities of 161, 137, 115, 90, 73, 64, 57, 49, and 38 mAh g^{-1} at 0.05, 0.1, 0.2, 0.5, 1.0, 1.5, 2.0, 3.0, and 5.0 A g^{-1}, respectively, as presented in Figure 3C (the corresponding dis-/charge profiles are provided in Supporting Information S1: Figure S6). When decreasing the specific current back to 0.1 A g^{-1}, the cells show a high capacity recovery of 98%, indicating a high structural stability of the electrode material.

The investigation of the electrochemical behavior of Sb-CeO_2 in Na-cells via CV is reported in Supporting Information S1: Figure S7. The voltammograms show a variegated electrochemical process where two cathodic peaks at 0.73 and 0.53 V versus Na^+/Na are identified in the initial cycle, accounting for electrolyte decomposition and SEI formation and the reduction of Ce and Sb, whereas the signal at around 0.04 V versus Na^+/Na indicates the insertion of Na^+ ions into the conductive carbon [30, 72, 73]. During the subsequent anodic scan, the de-insertion of the Na^+ ions from the carbon matrix is observed at 0.07 V versus Na^+/Na [73], followed by rather broad peaks located at 0.9 and 1.5 V versus Na^+/Na, corresponding to the extraction of Na^+ from the crystalline structure and the concomitant oxidation of Sb and Ce [30, 72]. The origin of the distinct peak observed at 2.1 V versus Na^+/Na might also be related to the reoxidation of the metal cations and/or a partial reoxidation of SEI components. Notably, the subsequent cycles evidence the stabilization of the Ce/Sb reduction processes at 1.3 and 0.4 V versus Na^+/Na, whereas the corresponding oxidation reactions appear to take place largely at around 0.9 V versus Na^+/Na, with several additional broad anodic features between 1.4 and 2.7 V

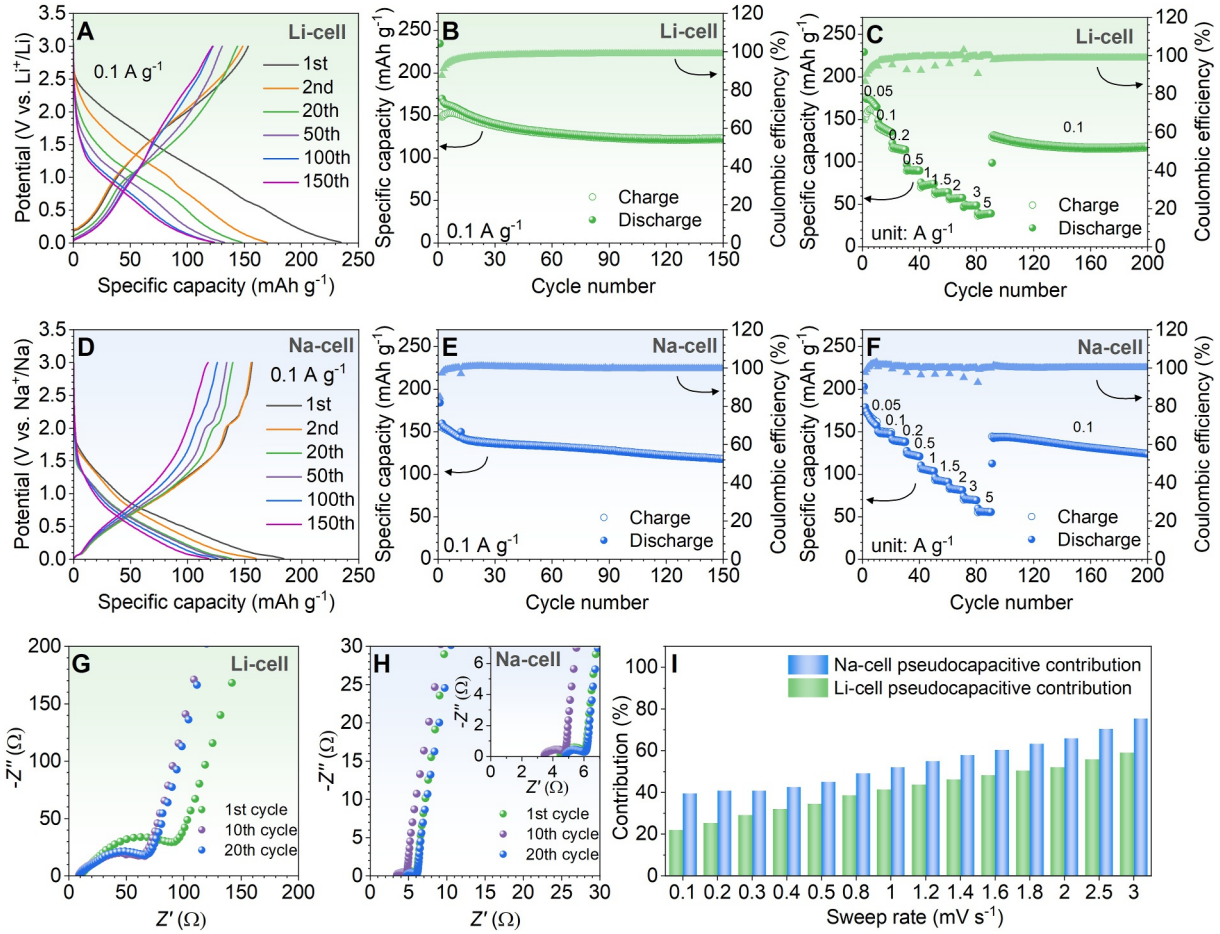

FIGURE 3 | Electrochemical characterization of Sb-CeO_2 electrodes in Li-cells and Na-cells. (A) Selected dis-/charge profiles and (B) capacity trend as a function of the cycle number recorded at 0.1 A g^{-1} in Li-cells. (C) Rate capability test performed on Li-cells between 0.05 and 5 A g^{-1}. (D) Selected dis-/charge profiles and (E) capacity trend as a function of the cycle number recorded at 0.1 A g^{-1} in Na-cells. (F) Rate capability test performed on Na-cells between 0.05 and 5 A g^{-1}. EIS spectra recorded during the cycling of (G) Li-cells and (H) Na-cells in the 200–0.01 kHz frequency range (voltage amplitude: 10 mV). (I) Comparison of the pseudocapacitive contribution at various CV sweep rates in Li-cells and Na-cells (the corresponding voltammograms are shown in Supporting Information S1: Figure S11).

versus Na^+/Na [30]. The galvanostatic dis-/charge profiles of the Na‖Sb-CeO_2 cells recorded at 0.1 A g^{-1} (Figure 3D) display an initial discharge and charge capacity of 184 and 156 mAh g^{-1}, respectively, resulting in a CE of 85%, indicating less irreversible side reactions in the first cycle compared to the Li-cell. In addition, the subsequent cycles reveal a relatively mild shape change of the voltage profiles, whereas the cycling trend depicted in Figure 3E shows a CE approaching 100% after the first few cycles, and a final charge capacity of 118 mAh g^{-1} after 150 cycles, with a capacity retention of 75%. Differently, the sodium storage properties of the CeO_2 reference electrodes, displayed in Supporting Information S1: Figure S8, show a maximum charge capacity of around 100 mAh g^{-1} and a capacity retention of 82% upon completing 100 cycles, which is very comparable with the capacity retention of Sb-CeO_2 after the same number of cycles (ca. 80%). Remarkably, the Na‖Sb-CeO_2 cells exhibit an improved rate capability with respect to the analogous Li-cells (Figure 3F), as demonstrated by the delivered charge capacities of 169, 150, 140, 123, 108, 92, 82, 70, and 56 mAh g^{-1} at 0.05, 0.1, 0.2, 0.5, 1, 1.5, 2, 3, and 5 A g^{-1}, respectively (the corresponding dis-/charge profiles are shown in Supporting Information S1: Figure S9). Given that the rate performance is also strongly affected by the choice of the electrolyte system, we conducted a control experiment using 1M $NaPF_6$ in EC/DEC as the electrolyte for the Na-cells (Supporting Information S1: Figure S10). In this case, the Sb-CeO_2 electrode exhibits a markedly inferior rate capability, accompanied by a low initial CE of 60%, and increased polarization compared with its behavior in the ether-based electrolyte. This behavior is consistent with previous reports indicating less favorable interfacial kinetics in carbonate-based electrolytes for SIBs [74, 75]. Together, these results indicate that optimizing the electrolyte system and the resulting interfacial chemistry are crucial to improve the initial (and average) CE and rate performance [76].

The reactions at the electrode | electrolyte interface for both Li-cells and Na-cells were investigated by EIS, as reported in Figure 3G,H, respectively. The NLLS analyses of the Nyquist plots recorded after the 1st, 10th, and 20th cycle at 0.1 A g^{-1} are presented in Table 1, where the Li-cells and Na-cells are described by $R_e(R_1Q_1)(R_2Q_2)(R_wQ_w)$ and the $R_e(R_1Q_1)Q_g$ equivalent circuits, respectively, composed of (i) R_e, derived from the high-frequency intercept of the Nyquist plot, representing the electrolyte resistance, (ii) R_i, the interphase resistance derived from the middle-

TABLE 1 | NLLS analyses performed on the Nyquist plots reported in were recorded on Li‖Sb-CeO_2 and Na‖Sb-CeO_2 cells upon cycling at 0.1 A g^{-1}.

Cell type	Condition	Equivalent circuit	R_1 (Ω)	R_2 (Ω)	R_i ($R_1 + R_2$) (Ω)	χ [2]
Li-cell	After 1 cycle	$R_e(R_1Q_1)(R_2Q_2)Q_w$	14.2 ± 0.8	68.6 ± 1.1	82.8 ± 0.9	2×10^{-5}
	After 10 cycles	$R_e(R_1Q_1)(R_2Q_2)Q_w$	11.1 ± 1.1	46.7 ± 1.8	57.8 ± 1.5	5×10^{-5}
	After 20 cycles	$R_e(R_1Q_1)(R_2Q_2)Q_w$	11.8 ± 0.7	48.7 ± 1.1	60.5 ± 0.9	2×10^{-5}
Na-cell	After 1 cycle	$R_e(R_1Q_1)Q_g$	1.66 ± 0.02	—	1.66 ± 0.02	2×10^{-5}
	After 10 cycles	$R_e(R_1Q_1)Q_g$	1.44 ± 0.03	—	1.44 ± 0.03	5×10^{-5}
	After 20 cycles	$R_e(R_1Q_1)Q_g$	1.46 ± 0.04	—	1.46 ± 0.04	3×10^{-5}

frequency semicircles' width and measured by the sum of the R_n elements ($n = 1, 2$) set in parallel with the capacitive Q_n elements, and (iii) either Q_w, the infinite Warburg-type ion diffusion determined from the low-frequency tilted line, or Q_g, the geometric cell capacitance defined by the high-frequency vertical line [48, 49]. The analyses reveal an initial interfacial resistance of 83 Ω for the Li-cells after the first cycle that decreases to ~60 Ω in the following ones, whereas the Na-cells exhibit very low values below 2 Ω in the considered cycling range. The NLLS results confirm the improvement of the kinetics upon cycling for the Li-cells, as discussed in Supporting Information S1: Figure S4 and Figure 3A,B, as well as the superior conductivity of the interphase formed in Na-cells, which well matches the better rate capability with respect to the Li-cells. A further understanding of the difference in kinetics related to the Sb-CeO_2 electrodes in Li-cells and Na-cells is provided by the determination of the contribution of the nondiffusion-controlled (i.e., pseudo-/capacitive) charge storage to the general electrochemical process. Supporting Information S1: Figure S11 shows the CV data obtained for Sb-CeO_2 in Li-cells (Supporting Information S1: Figure S11A,B) and Na-cells (Supporting Information S1: Figure S11C,D) at various sweep rates ranging from 0.1 to 3.0 mV s^{-1}. The pseudo-/capacitive contribution was calculated using Equation (1) [77, 78]:

$$i(V) = k_1 v + k_2 v^{1/2}, \quad (1)$$

where $i(V)$ is the current recorded at the specific potential (V) and v is the sweep rate. The diffusion-controlled and pseudo-/capacitive contributions of the electrochemical process can be quantified by $k_2v^{1/2}$ and k_1v, respectively, where k_1 and k_2 are determined from the slope and the intercept of the $i(V)/v^{1/2}$ versus $v^{1/2}$ plot [77, 78]. The contribution of the pseudo-/capacitive process calculated from the CV data at different sweep rates is displayed in Figure 3I. The analysis reveals a higher pseudo-/capacitive contribution for the Na-cells compared to the Li-cells, with values increasing from 39% to 75% for the former and from 22% to 59% for the latter between 0.1 and 3.0 mV s^{-1}. This might be (in part) related to the rather different interfacial reactions of the two systems—in the case of the Na-cells benefiting from the very low interfacial resistance—and provides an explanation for the superior rate capability of the Na-cells.

3.3 | Comprehensive Study of the Reaction Mechanism

To investigate the structural evolution of Sb-CeO_2 during cycling in Li-cells and Na-cells, a comprehensive analysis of the electrodes was performed by operando XRD and ex situ XAS, as depicted in Figure 4. Figure 4A–C shows the operando XRD patterns of Sb-CeO_2 collected during the first two cycles in Li-cells (Figure 4A) along with the corresponding waterfall diagram (Figure 4B) and dis-/charge profiles (Figure 4C). The intensity of the XRD reflections slightly decreases during the lithiation process in concomitance to the shift of the peaks to lower 2θ degrees, indicating the enlargement of the unit cell during the discharge process until about 1.0 V, whereas below this value, all the reflections of Sb-CeO_2 remain nearly unchanged in both peak position and symmetry, indicating the stability of the cell unit and structure. Upon the following charging process, a shift back to the original 2θ values occurs at voltages above 1.0 V, confirming the remarkable structural integrity of Sb-CeO_2 upon repeated cycling. Moreover, no other phase except the one related to cubic CeO_2 is detected during cycling, being well in line with a solid solution-type reaction during the de-/lithiation process, as observed earlier for Fe-doped CeO_2 [28].

The same evaluation was performed for Na-cells, as presented in Figure 4D–F. The operando XRD characterization (Figure 4D,E) reveals a constant shift of the reflections to lower 2θ values during the whole sodiation process and a shift back to the original position and intensity in the fully desodiated state (Figure 4F), indicating that, also in this case, the crystal structure of Sb-CeO_2 is well maintained. Again, no new phases are observed other than the one for cubic CeO_2. Overall, the operando XRD results demonstrate the structural reversibility of the CeO_2 host framework in Sb-CeO_2 during electrochemical cycling in both Li-cells and Na-cells.

The investigation of the chemical states of Ce and Sb in Sb-CeO_2 during dis-/charge was conducted by ex situ XAS, specifically XANES, as displayed in Figure 4G–J. Figure 4G presents the Ce L_{III}-edge spectra of Sb-CeO_2 discharged to 0.01 V in Li-cells and Na-cells, alongside the spectra of pristine Sb-CeO_2, CeO_2, and $Ce_2(SO_4)_3$ serving as references. Upon discharge to 0.01 V, cerium in Sb-CeO_2 is reduced from Ce^{4+} to Ce^{3+}, as indicated by the edge shift toward values approaching that of $Ce_2(SO_4)_3$. The position of the Ce L_{III}-edge for the electrode discharged in Li-cells is located at a slightly lower energy compared to that of the electrode discharged in Na-cells, indicating a more pronounced reduction of Ce^{4+} to Ce^{3+}, which is in line with the higher capacity and can be assigned to the larger ionic radius of Na^+ and the resulting space requirement in the crystal structure. Interestingly, the Ce L_{III}-edge of the Sb-CeO_2 electrodes in Li-cells (Figure 4H) shows a significantly greater shift back after recharge to 3.0 V, close to the peak position of pristine CeO_2,

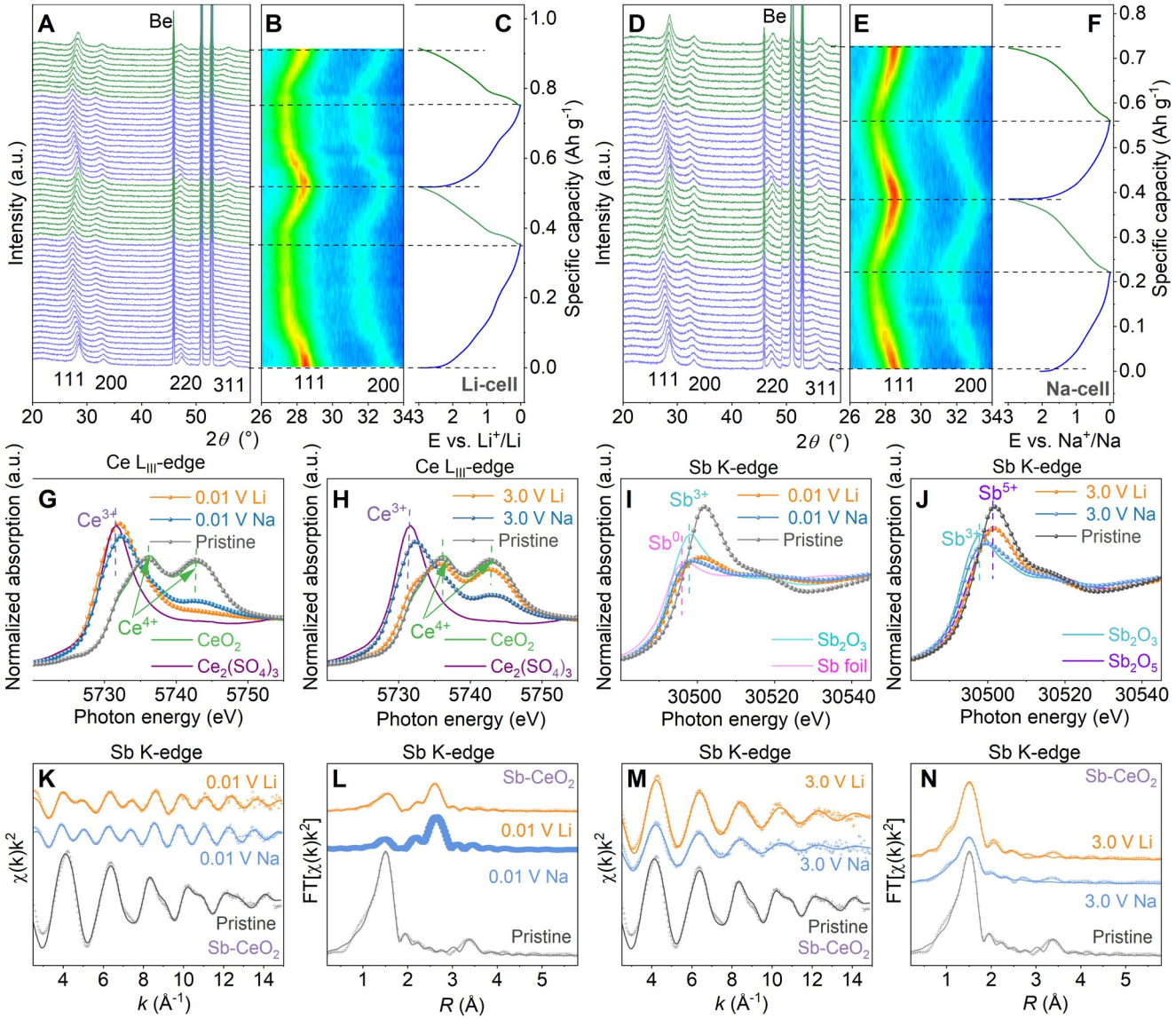

FIGURE 4 | Bulk-sensitive investigation of the charge storage mechanism. Operando XRD analysis of Sb-CeO_2 electrodes during the first two cycles in (A–C) Li-cells and (D–F) Na-cells: (A, D) waterfall diagrams, (B, E) contour plots with blue and red indicating minimum and maximum XRD reflection intensities, respectively, and (C, F) the corresponding dis-/charge profiles. (G, H) Ce L_{III}-edge and (I, J) Sb K-edge XAS spectra recorded for (G, I) Sb-CeO_2 electrodes discharged to 0.01 V and (H, J) for Sb-CeO_2 electrodes either at the pristine state or charged to 3.0 V in Li-cells and Na-cells. (K–N) Ex situ EXAFS spectra and corresponding multiparameter fit for pristine and dis/-charged Sb-CeO_2 ("+" denotes experimental data; the solid lines represent the fitting results). (K, M) The Sb K-edge k^2-weighted EXAFS region of Sb-CeO_2 electrodes (K) discharged to 0.01 V and (M) charged to 3.0 V. (L, N) The Fourier transforms of the EXAFS for the Sb-CeO_2 electrodes (L) discharged to 0.01 V and (N) charged to 3.0 V.

indicating a very reversible redox reaction of Ce, whereas the edge of the electrode cycled in Na-cells remained at a somewhat lower energy, suggesting a relatively limited oxidation of Ce.

Similarly, the Sb K-edge spectra of the Sb-CeO_2 electrodes discharged to 0.01 V in Li-cells and Na-cells (Figure 4I, Supporting Information S1: Figure S12A) reveal that Sb is largely reduced in both cases, essentially to its metallic state, as confirmed by comparing the spectra with the spectrum recorded for Sb metal foil. The same indication is provided by the EXAFS analysis (Figure 4K,L, Supporting Information S1: Table S3) where the signal is dominated by an Sb-Sb scattering path with interatomic distances (2.81 and 2.84 Å for the lithiated (0.01 V Li) and sodiated (0.01 V Na) samples, respectively) slightly shorter than those typical of elemental Sb (2.84 Å), but in line with previous findings for Fe-doped CeO_2 [28], while also a minor contribution from Sb-O interaction observed, further highlighting the atom-level reduction of Sb in this structure. Also in this case, the reoxidation to Sb^{5+} appears more pronounced for the electrodes cycled in Li-cells upon charge to 3.0 V, as indicated by the comparison with the spectrum recorded for Sb_2O_5, whereas it remains incomplete for the electrodes cycled in Na-cells (Figure 4J, Supporting Information S1: Figure S12B), indicating an oxidation state between +3 and +5 (see the comparison with the spectra obtained for Sb_2O_3 and Sb_2O_5). The very similar Sb-O bond distances revealed by EXAFS (Figure 4M,N,

Supporting Information S1: Table S3) in pristine, delithiated (3.0 V Li) and desodiated (3.0 V Na) samples indicate, from a structural perspective, the reversibility of the reaction. In the desodiated sample, however, the lower amplitude reduction factor (S_0^2), together with the higher Debye–Waller factor (σ^2), indicates some additional disorder in the local structure of Sb, in agreement with the mixed-valence suggested by the XANES analysis. These results reveal a generally higher reversibility for the de-/lithiation process compared to the de-/sodiation process, which agrees well with the higher specific capacity and capacity retention observed for the Li-cells.

In order to obtain a deeper understanding of the reaction mechanism and the differences observed for Li and Na, a detailed investigation of the surface chemistry of the Sb-CeO_2 electrode was performed using ex situ soft-XAS in total electron yield (TEY) and total fluorescence yield (TFY) mode to provide valuable information at different probing depths. Figure 5A,B shows the TEY Ce M-edge spectra of the pristine Sb-CeO_2 electrode and the ones cycled in Li-cells (Figure 5A) and Na-cells (Figure 5B). The results reveal that the intensity of the Ce-related peaks substantially decreases upon discharge to 0.01 V, which is attributed to the formation of an SEI layer at the electrode surface [79]. When subsequently charging the cells to 3.0 V, though, the intensity of the Ce-related peaks increases again—in particular for the Li-cells, indicating that the SEI is largely dissolved/re-oxidized. For the Na-cells, this increase is substantially less pronounced, suggesting that the SEI is much more stable in this case. After 50 cycles (at 3.0 V), the Ce-related peaks exhibit a general decrease in intensity in both cases, which can be explained by the gradual growth and thickening of the SEI over cycling. It is worth noting that for the Ce M-edge signals in TEY mode, the features of Ce^{3+} are more intense than those of Ce^{4+}, regardless of the state of charge of the electrodes, which is due to the reduction of Ce^{4+} to Ce^{3+} upon exposure of the samples to the experimental conditions and radiation [61, 80, 81].

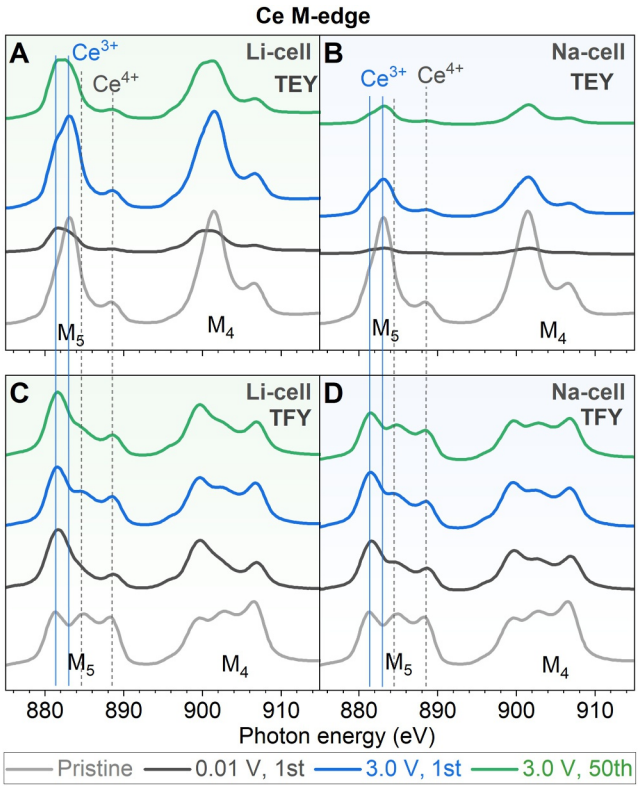

FIGURE 5 | Surface-sensitive investigation of the charge storage mechanism. Ce M-edge soft-XAS spectra in (A, B) TEY and (C, D) TFY mode of pristine and cycled Sb-CeO_2 electrodes retrieved either from (A, C) Li-cells or (B, D) Na-cells after the 1st discharge to 0.01 V, the 1st charge to 3.0 V, and the 50th charge to 3.0 V.

Figure 5C,D shows the Ce M-edge spectra collected in TFY mode, which provides information from deeper probing depths, reducing the signal contribution from the outer SEI with respect to the TEY mode. Generally, they confirm the reduction to Ce^{3+} upon discharge to 0.01 V in the Li-cell (Figure 5C) and the reoxidation to Ce^{4+} upon charge to 3.0 V, although with a slightly lower intensity compared to the pristine state, indicating a partially incomplete reoxidation and/or the earlier mentioned sample damage. In fact, the spectra recorded after the 50th charge show a further decrease of the Ce^{4+} peak intensity, indicating the partial suppression of the Ce^{3+}/Ce^{4+} redox activity during cycling, which is in agreement with the gradual capacity decay observed in Figure 3B. Likewise, the first discharge of the Na-cell (Figure 5D) causes the reduction of Ce^{4+} to Ce^{3+}; however, the extent of this reduction is smaller than that observed in the Li-cell, consistent with the XAS results presented in Figure 4G,H. After 50 cycles, there is little difference observed compared to the charged state after the first complete cycle, further supporting the conclusion that the SEI is significantly more stable in the case of Na.

The chemical composition of the SEI at the Sb-CeO_2 electrode surface has been analyzed by taking a closer look at the C, F, O, Li, and Na K-edges (Figure 6). The Li, C, and Na K-edges have been analyzed only in TEY mode, whereas O and F have also been analyzed in TFY mode. Figure 6A displays the C K-edge soft-XAS spectra of Sb-CeO_2 electrodes cycled in Li-cells, revealing that the EC/DEC solvents decompose during the first discharge at 0.01 V to form Li_2CO_3 (290.2, 297.1, and 300.4 eV) and $ROCO_2Li$ (288.4 eV) species in the outer region of the SEI layer [79, 82–84]. The intensity of these components decreases after the 1st charge at 3.0 V, yet after 50 cycles, they are higher in the charged state, supporting the earlier observation of an initial dissolution of the SEI during the first charge and its subsequent consolidation throughout cycling. Similarly, the TEY C K-edge spectra reported in Figure 6B collected for the Sb-CeO_2 electrodes cycled in Na-cells with an electrolyte comprising DME as solvent show an SEI layer dominated by Na_2CO_3 (290.1, 297.5, and 300.6 eV) with minor amounts of sodium alkoxides such as RCH_2ONa or RONa (288.8 eV) after the first discharge to 0.01 V [85, 86]. The predominance of Na_2CO_3 demonstrates that the decomposition of such ether-based electrolyte favors the formation of an inorganic-rich interphase. Importantly, these features decrease only slightly upon charge and there is also very little change after 50 cycles, corroborating the superior stability of the SEI formed in Na-cells compared to Li-cells.

At the TEY Li K-edge (Figure 6C), the 1st discharge yields pronounced $ROCO_2Li$-related features (59.8, 65.1 eV) and a weaker Li_2CO_3 peak (61.7 eV) [87, 88]. After subsequent charging to 3.0 V, these features decrease, whereas LiF-related features appear at

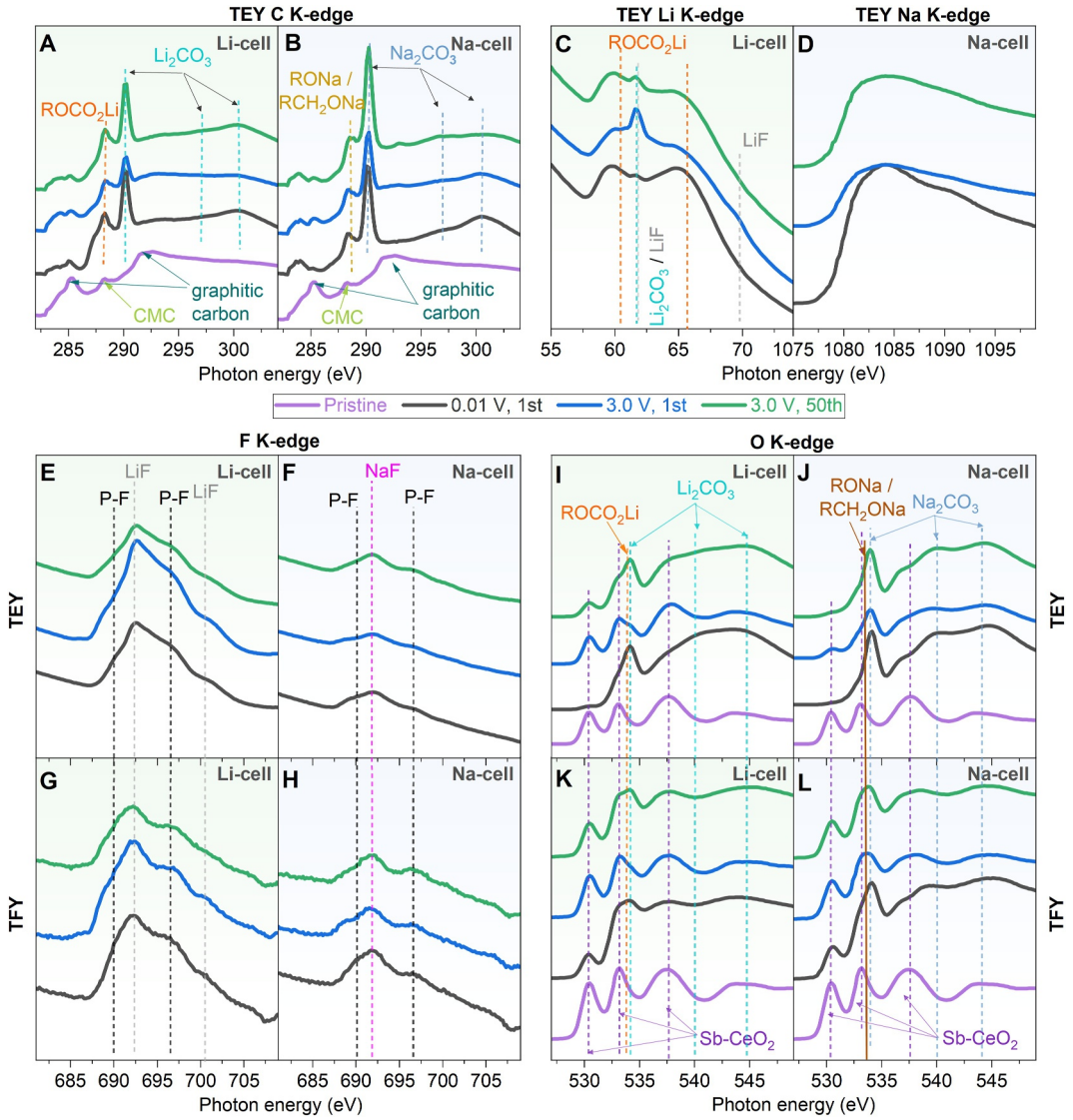

FIGURE 6 | Investigation of the reactions occurring at the electrode | electrolyte interface. Soft-XAS spectra of Sb-CeO_2 electrodes at the pristine state and electrodes retrieved from (A, C, E, G, I, K) Li-cells and (B, D, F, H, J, L) Na-cells after the 1st discharge to 0.01 V, the 1st charge to 3.0 V, and the 50th charge to 3.0 V: (A, B) TEY C K-edge spectra, (C) TEY Li K-edge spectra, (D) TEY Na K-edge spectra, (E–H) F K-edge spectra in (E, F) TEY and (G, H) TFY mode, and (I–L) O K-edge spectra in (I, J) TEY and (K, L) TFY mode.

61.7 and 69.8 eV, indicating the partial dissolution of the outer carbonate/organic layer and exposure of an inner LiF-rich layer. After 50 cycles, the carbonate-related peaks increase again, whereas LiF appears attenuated in the TEY spectra, presumably as it is covered by other species in an outer layer. These results reveal a dynamic SEI in Li-cells, undergoing repeated dissolution and re-accumulation. The Na K-edge spectra (Figure 6D) display a different evolution: After the first discharge, very broad, essentially indistinguishable features above 1077 eV are observed, presumably comprising Na_2CO_3 and NaF [89]. Upon charging to 3.0 V, the intensity decreases slightly, reflecting a partial dissolution of such Na-containing species. However, after 50 cycles, the broad peak increases again in intensity, demonstrating a consolidation of the SEI, though much less pronounced than in the case of the Li-cells.

The F K-edge could better support the evolution of NaF/LiF during the cycling process. The TEY F K-edge spectra for cycled electrodes in Li-cells (Figure 6E) show an increase in intensity for the LiF-related peaks (692.5 eV) after the 1st charge to 3.0 V owing to the dissolution of the outer SEI, indicating that LiF predominantly contributes to the inner layers of the SEI film and remains rather stable upon charging, which is consistent with previous reports [90]. After 50 cycles, a reduction in intensity is observed, which can be attributed to the rebuilding of the outer SEI layer, masking the inner F signal. The same behavior is observed for the P-F species (690.0 and 696.5 eV), likely derived from residual $LiPF_6$ degradation products [91, 92]. The significantly higher intensity of the LiF-related peaks compared to those of $LiPF_6$ and $LiPF_x$ suggests that LiF is the dominant F-containing component within the SEI inner layer. The TEY F K-edge spectra for electrodes cycled in Na-cells demonstrate a somewhat different peak evolution over the cycling process (Figure 6F). In detail, the NaF signal (692.0 eV) slightly decreases after the first charge to 3.0 V and increases again after 50 cycles, indicating the presence of NaF also in the external layer of the SEI, unlike LiF [91]. Notably, the

intensities of the F K-edge spectra in the case of the Na-cells display a rather minimal variation throughout cycling, indicating a much more stable SEI layer than the one formed in Li-cells. This stability suggests that the SEI in Na-cells is less prone to continuous growth and reformation, potentially contributing to the lower impedance. Deeper probing via the TFY mode (Figure 6G,H) still shows LiF/NaF with a similar evolution to that in the TEY mode. Figure 6I,J shows the spectra of TEY O K-edge for cycled electrodes in Li-cells and Na-cells, respectively. In both cases, prominent features appear at 533.6 eV, corresponding to the formation of alkyl carbonates, such as $ROCO_2Li$, or sodium alkoxides, such as RCH_2ONa or RONa. Additionally, features at 533.9, 540.1, and 544.7 eV are observed, which are consistent with the formation of Li_2CO_3 in Li-cells and Na_2CO_3 in Na-cells [83, 86, 89]. Besides, Sb-CeO_2-related peaks (O K-edge and Sb M-edge) can be observed in the range from 530 to 537 eV [93]. When discharged to 0.01 V, the Sb-CeO_2-related peaks vanish and peaks related to Li_2CO_3 (Li-cells) and Na_2CO_3 (Na-cells) become more pronounced, indicating the formation of the SEI layer. When charged to 3.0 V, the Sb-CeO_2-related peaks partially reappear in Li-cells, in line with a partial dissolution of the SEI layer on the electrode surface. For the Na-cells, the reappearance of the Sb-CeO_2-related peaks is substantially less pronounced, further corroborating the formation of a more stable SEI layer in Na-cells. After 50 cycles, the features related to Li_2CO_3 and $ROCO_2Li$ or Na_2CO_3 and sodium alkoxides still show up in both Li-cells and Na-cells; and although the Sb-CeO_2-related peaks are still observed for the Li-cells, they are almost not visible anymore for the Na-cells.

The TFY spectra at the O K-edge (Figure 6K,L) provide further insights into the SEI evolution. Different from the TEY spectra, despite discharging to 0.01 V, the Sb-CeO_2-related peaks are still detectable in both cases, indicating that the thickness of the SEI layer is less than the average TFY probing depth at the O K-edge.

The composition of the SEI and its evolution in Na-cells was further examined by ex situ XPS (Supporting Information S1: Figure S13). Essentially, the same peaks are observed for the Sb-CeO_2 electrodes after the first discharge to 0.01 V, the first charge to 3.0 V, and after 50 cycles in the charged state. The C 1s signal at 284.8 eV is assigned to C-C and C-H species, the peak at 286.4 eV is attributed to the C-O bond, which may arise from ether fragments and sodium alkoxides (RONa, RCH_2ONa), and the peaks at 288.2 and 290.1 eV are attributed to O-C=O and CO_3 bonds, respectively, originating from alkyl carbonates and Na_2CO_3 species (Supporting Information S1: Figure S13A) [73, 94]. The slight decrease of the Na_2CO_3 signal after charge to 3.0 V aligns with the TEY C K-edge soft-XAS results, indicating a partial dissolution upon charge and stabilization upon cycling. This evolution is confirmed by the comparison of the Na_2CO_3 signal in the Na 1s spectra (Supporting Information S1: Figure S13B), showing exactly the same trend. The NaF peak at about 1071 eV displays only very minor changes upon cycling, confirming at the same time its presence throughout the SEI and its greater robustness compared to the Li-cells.

Overall, combining the soft-XAS and XPS results shows that the SEI in the Li-cells is comprised of $ROCO_2Li$, Li_2CO_3, and LiF with a dynamic outer layer and a relatively stable inner LiF-rich layer, whereas for the Na-cells, a relatively inorganic-rich SEI is formed, dominated by Na_2CO_3 with minor amounts of Na-alkoxides and more uniformly distributed NaF, with the SEI in the Na-cells being favorable for the interfacial charge transport (along with a lower Na^+ desolvation barrier in the DME-based electrolyte) [95], as revealed earlier by EIS. The evolution of the SEI layer on the electrode surface during cycling in Li-cells and Na-cells is schematically summarized in Supporting Information S1: Figure S14.

3.4 | Evaluation in Sb-CeO_2 ‖ $Na_3V_2(PO_4)_3$ Full-Cells

To finally evaluate the performance in full-cells, we studied exemplarily the combination with NVP-based positive electrodes in sodium-ion full-cells. NVP was selected as the counter electrode active material because of its excellent rate capability up to 50C (Supporting Information S1: Figure S15A,B) and cycling stability with a very good capacity retention of 98% after 500 cycles (Supporting Information S1: Figure S15C,D), matching the very good rate capability of the Sb-CeO_2 in Na half-cells. The Sb-CeO_2 ‖ NVP full-cells were assembled with an N/P ratio of 1.1 and the results are presented in Figure 7. Figure 7A,B shows the results of the rate capability test with selected dis-/charge profiles displayed in Figure 7A and the plot of the specific capacity versus the cycle number in Figure 7B. The shape of the dis-/charge profiles reflects the combination of the shape of the two electrodes and the cell has an average cell voltage of about 2.2 V at 1C, whereas elevated C rates lead to an increasing overpotential for the charge and discharge process—as commonly expected. Nonetheless, at a very high C rate of 50C, the cells still provide about 50% of the capacity obtained at 1C, revealing an excellent rate capability and power performance. More precisely, the cells show a specific discharge capacity of 112, 101, 93, 86, 77, 68, 62, and 55 mAh g^{-1} at 1C, 2C, 3C, 5C, 10C, 20C, 30C, and 50C, respectively (based on the mass of the Sb-CeO_2 negative electrode; see Supporting Information S1: Figure S16 for the same plots based on the mass of the NVP positive electrode), which is even more remarkable considering that the cells and the N/P ratio have not yet been optimized in any way. When the C rate is decreased back to 1C after 80 cycles, the discharge capacity reaches 93 mAh g^{-1}, corresponding to 83% of the initial value.

Additionally, cells were subjected to a constant current cycling at a very high C rate of 20C and the results are presented in Figure 7C,D. The evolution of the corresponding dis-/charge profiles reveals a slight increase in polarization upon cycling, along with a slight "shortening" of the dis-/charge profiles, suggesting a loss of capacity, presumably originating from the loss of electrochemically active lithium owing to the still-to-be-optimized stability at the electrode | electrolyte interface(s). This is further corroborated by the analysis of the corresponding dQ/dV plots, revealing a slight shift of the peak maxima and decrease in current intensity (Supporting Information S1: Figure S17). These findings suggest that the interfaces may still benefit from further stabilization—for instance, by optimizing the electrolyte composition and/or applying protective coatings. Nonetheless, the Sb-CeO_2 ‖ NVP full-cells show a rather stable performance for about 200 cycles with a capacity retention of 73% and an average CE of around 99.8% (Figure 7D), confirming that this new class of anode materials, containing highly redox-

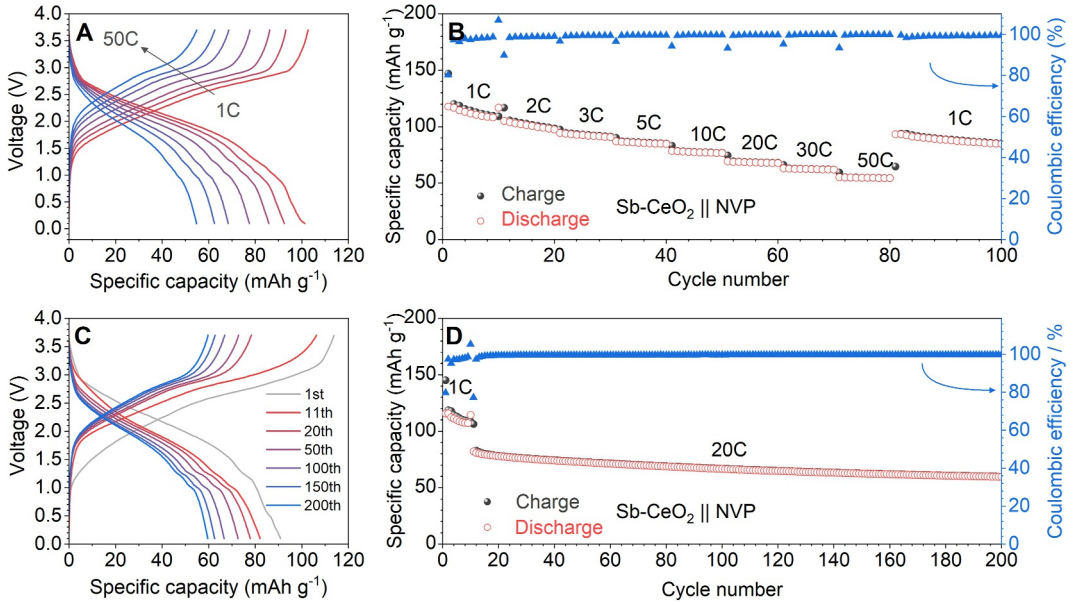

FIGURE 7 | Electrochemical characterization of Sb-CeO_2‖NVP Na-ion full-cells with an N/P ratio of around 1.1. (A, C) Selected voltage profiles and (B, D) specific capacity as a function of cycle number related to (A, B) a rate capability test and (C, D) long-term galvanostatic cycling at a constant C rate of 20C after 10 activation cycles at 1C (1C = 120 mA g^{-1}; voltage range: 0.1–3.7 V). The specific capacity of the full-cell is calculated based on the mass of the Sb-CeO_2 anode active material (see Supporting Information S1: Figure S16 for the same plot with the specific capacity of the full-cell being calculated based on the mass of the NVP cathode active material).

active atomic centers in an insertion-type host framework, indeed, provides an excellent power performance and offers the possibility to rapidly charge the cells at very high C rates.

4 | Conclusions

The partial substitution of Ce by Sb in cubic CeO_2 results in substantially increased specific capacities and an enhanced cycling stability in Li-cells and Na-cells. Operando XRD and ex situ XAS reveal pronounced lithium/sodium insertion into the cubic crystal structure along with the reduction of the antimony dopant to the metallic state upon lithiation/sodiation, rendering this material very versatile concerning a potential application in these two different battery technologies. Interestingly, the capability to host lithium cations is greater than for sodium cations, suggesting that there is a "size effect", that is, that there is simply more room for the smaller lithium cations in the host structure, whereas the interfacial resistance in the Na-cells is significantly smaller—presumably also owing to the different nature of the electrolyte used, yielding a better rate capability despite the somewhat thicker (and more stable) SEI formed at the electrode surface, as evidenced by ex situ soft-XAS and XPS experiments. Finally, the combination of Sb-CeO_2 with NVP cathodes in Na-ion full-cells confirms the excellent fast charging capability up to a very high C rate of 50C, underlining the suitability of this new reaction mechanism for high-power rechargeable batteries.

Author Contributions

Yunjie Li: data curation, formal analysis, investigation, methodology, validation, visualization, writing – original draft. **Xilai Xue:** data curation, formal analysis, investigation, methodology, validation, visualization, writing – review and editing. **Seyed Javad Rezvani:** data curation, formal analysis, investigation, methodology, writing – review and editing, resources. **Giovanni Orazio Lepore:** conceptualization, data curation, formal analysis, investigation, methodology, writing – original draft, writing – review and editing, resources. **Holger Euchner:** data curation, formal analysis, investigation, writing – review and editing, methodology. **Angelo Giglia:** data curation, formal analysis, investigation, writing – review and editing, methodology, resources. **Thomas Diemant:** data curation, formal analysis, investigation, validation, writing – review and editing. **Yueliang Li:** data curation, formal analysis, investigation, writing – review and editing. **Ute Kaiser:** formal analysis, methodology, resources, supervision, writing – review and editing. **Dariusz Mitoraj:** data curation, formal analysis, visualization, writing – review and editing, investigation. **Radim Beranek:** investigation, methodology, resources, supervision, writing – review and editing. **Argjend Blakaj:** data curation, formal analysis, investigation, writing – review and editing. **Alessandro Puri:** data curation, formal analysis, writing – review and editing. **Francesco d'Acapito:** methodology, resources, supervision, writing – review and editing. **Vittorio Marangon:** investigation, methodology, project administration, supervision, visualization, writing – review and editing. **Dominic Bresser:** conceptualization, funding acquisition, investigation, methodology, resources, supervision, writing – review and editing.

Acknowledgments

Financial support for this study was provided by the European Research Council (ERC), within the RACER (Project 10143029). Views and opinions expressed are those of the authors only and do not necessarily reflect those of the European Union or the ERC. Neither the European Union nor the granting authority can be held responsible for them. Additionally, the authors would like to acknowledge financial support from the Helmholtz Association. The authors also gratefully acknowledge CERIC ERIC for beamtime allocation at the LISA-BM08 beamline at the ESRF (exp. No. 20232190, a08-1-1107). LISA is funded by the Consiglio Nazionale delle Ricerche through project DFM.AD006.072. We also thank Elettra Sincrotrone Trieste for providing access to its synchrotron radiation facilities. Furthermore, the study linked to Proposal No. 20235031 received additional support from the NEPHEWS

project (Grant No. 101131414) within the EU Framework Program for Research and Innovation Horizon Europe. Open Access funding enabled and organized by Projekt DEAL.

Conflicts of Interest

The authors declare no conflicts of interest.

Data Availability Statement

The data that support the findings of this study are available from the corresponding author upon reasonable request.

References

1. J. B. Goodenough and K. S. Park, "The Li-Ion Rechargeable Battery: A Perspective," *Journal of the American Chemical Society* 135, no. 4 (2013): 1167–1176, https://doi.org/10.1021/ja3091438.

2. E. Goikolea, V. Palomares, S. Wang, et al., "Na-Ion Batteries—Approaching Old and New Challenges," *Advanced Energy Materials* 10, no. 44 (2020): 2002055, https://doi.org/10.1002/aenm.202002055.

3. F. M. N. U. Khan, M. G. Rasul, A. S. M. Sayem, and N. K. Mandal, "Design and Optimization of Lithium-Ion Battery as an Efficient Energy Storage Device for Electric Vehicles: A Comprehensive Review," *Journal of Energy Storage* 71 (2023): 108033, https://doi.org/10.1016/j.est.2023.108033.

4. C. Vaalma, D. Buchholz, M. Weil, and S. Passerini, "A Cost and Resource Analysis of Sodium-Ion Batteries," *Nature Reviews Materials* 3, no. 4 (2018): 18013, https://doi.org/10.1038/natrevmats.2018.13.

5. V. Marangon, K. Bischof, A. A. Regalado, et al., "Cell Design and Chemistry of Commercial Sodium-Ion Battery Cells," *Journal of Power Sources* 634 (2025): 236496, https://doi.org/10.1016/j.jpowsour.2025.236496.

6. H. S. Hirsh, Y. Li, D. H. S. Tan, M. Zhang, E. Zhao, and Y. S. Meng, "Sodium-Ion Batteries Paving the Way for Grid Energy Storage," *Advanced Energy Materials* 10, no. 32 (2020): 2001274, https://doi.org/10.1002/aenm.202001274.

7. X. Li, X. Sun, X. Hu, et al., "Review on Comprehending and Enhancing the Initial Coulombic Efficiency of Anode Materials in Lithium-Ion/Sodium-Ion Batteries," *Nano Energy* 77 (2020): 105143, https://doi.org/10.1016/j.nanoen.2020.105143.

8. W. Zhao, C. Zhao, H. Wu, L. Li, and C. Zhang, "Progress, Challenge and Perspective of Graphite-Based Anode Materials for Lithium Batteries: A Review," *Journal of Energy Storage* 81 (2024): 110409, https://doi.org/10.1016/j.est.2023.110409.

9. H. Zhang, Y. Yang, D. Ren, L. Wang, and X. He, "Graphite as Anode Materials: Fundamental Mechanism, Recent Progress and Advances," *Energy Storage Materials* 36 (2021): 147–170, https://doi.org/10.1016/j.ensm.2020.12.027.

10. W. Y. Qian, K. Y. Zhang, and X. L. Wu, "Post-Treatment-Induced Structural Reconstruction of Hard Carbon Toward Optimized Sodium Storage: A Perspective and Review," *Energy Storage Materials* 81 (2025): 104529, https://doi.org/10.1016/j.ensm.2025.104529.

11. X. Dou, I. Hasa, D. Saurel, et al., "Hard Carbons for Sodium-Ion Batteries: Structure, Analysis, Sustainability, and Electrochemistry," *Materials Today* 23 (2019): 87–104, https://doi.org/10.1016/j.mattod.2018.12.040.

12. J. Asenbauer, T. Eisenmann, M. Kuenzel, A. Kazzazi, Z. Chen, and D. Bresser, "The Success Story of Graphite as a Lithium-Ion Anode Material – Fundamentals, Remaining Challenges, and Recent Developments Including Silicon (Oxide) Composites," *Sustainable Energy Fuels* 4, no. 11 (2020): 5387–5416, https://doi.org/10.1039/D0SE00175A.

13. S. Tan, Y. Wen, J. Li, et al., "Fast-Charging Capabilities of Hard Carbon Anodes in Sodium-Ion Batteries: Mechanisms, Strategies, and Prospects," *Carbon Neutralization* 4, no. 6 (2025): e70071, https://doi.org/10.1002/cnl2.70071.

14. Y. Liu, H. Shi, and Z. S. Wu, "Recent Status, Key Strategies and Challenging Perspectives of Fast-Charging Graphite Anodes for Lithium-Ion Batteries," *Energy & Environmental Science* 16, no. 11 (2023): 4834–4871, https://doi.org/10.1039/D3EE02213G.

15. L. Sun, Y. Liu, R. Shao, J. Wu, R. Jiang, and Z. Jin, "Recent Progress and Future Perspective on Practical Silicon Anode-Based Lithium Ion Batteries," *Energy Storage Materials* 46 (2022): 482–502, https://doi.org/10.1016/j.ensm.2022.01.042.

16. J. He, Y. Wei, T. Zhai, and H. Li, "Antimony-Based Materials as Promising Anodes for Rechargeable Lithium-Ion and Sodium-Ion Batteries," *Materials Chemistry Frontiers* 2, no. 3 (2018): 437–455, https://doi.org/10.1039/C7QM00480J.

17. S. Liang, Y. J. Cheng, J. Zhu, Y. Xia, and P. Müller-Buschbaum, "A Chronicle Review of Nonsilicon (Sn, Sb, Ge)-Based Lithium/Sodium-Ion Battery Alloying Anodes," *Small Methods* 4, no. 8 (2020): 2000218, https://doi.org/10.1002/smtd.202000218.

18. M. N. Obrovac and V. L. Chevrier, "Alloy Negative Electrodes for Li-Ion Batteries," *Chemical Reviews* 114, no. 23 (2014): 11444–11502, https://doi.org/10.1021/cr500207g.

19. Z. Z. Yang, C. Y. Zhang, Y. Q. Ou, et al., "Amorphous Sb/C Composite With Isotropic Expansion Property as an Ultra-Stable and High-Rate Anode for Lithium-Ion Batteries," *Rare Metals* 43, no. 5 (2024): 2039–2052, https://doi.org/10.1007/s12598-023-02548-x.

20. D. Wang, Q. Ma, H. He, et al., "Double-Confined Nano-heterostructure $Sb/Sb_2S_3@Ti_3C_2T_x@C$ Toward Ultra-Stable Li-/Na-Ion Batteries," *Rare Metals* 43, no. 5 (2024): 2067–2079, https://doi.org/10.1007/s12598-023-02550-3.

21. J. Y. Ren, X. L. Yu, C. M. Chen, X. Y. Hu, T. Yang, and M. Zhang, "Pyridine-Regulated $Sb@InSbS_3$ Ultrafine Nanoplates as High-Capacity and Long-Cycle Anodes for Sodium-Ion Batteries," *Rare Metals* 43, no. 5 (2024): 2080–2092, https://doi.org/10.1007/s12598-023-02582-9.

22. Z. Yang, Q. L. Kang, L. J. Yan, X. H. Meng, T. L. Ma, and T.-Li Ma, "Structural Engineering of Sb-Based Electrode Materials to Enhance Advanced Sodium-Ion Batteries," *Rare Metals* 43, no. 10 (2024): 4777–4806, https://doi.org/10.1007/s12598-024-02730-9.

23. J. G. Deng, H. Q. Feng, Y. L. Xu, et al., "Metallic Sb-Stabilized Porous Silicon With Stable SEI and High Electron/Ion Conductivity Boosting Lithium-Ion Storage Performance," *Rare Metals* 43, no. 9 (2024): 4234–4242, https://doi.org/10.1007/s12598-024-02632-w.

24. C. Lin, G. Suo, R. Mu, et al., "Dual Carbon Confining SnO_2 Nanocrystals as High-Performance Anode for Sodium-Ion Batteries," *Journal of Power Sources* 623 (2024): 235426, https://doi.org/10.1016/j.jpowsour.2024.235426.

25. H. Liu, Z. Zhu, J. Huang, et al., "Elucidating the Limit of Li Insertion into the Spinel $Li_4Ti_5O_{12}$," *ACS Materials Letters* 1, no. 1 (2019): 96–102, https://doi.org/10.1021/acsmaterialslett.9b00099.

26. H. Zhang, Y. Yang, H. Xu, L. Wang, X. Lu, and X. He, "$Li_4Ti_5O_{12}$ Spinel Anode: Fundamentals and Advances in Rechargeable Batteries," *InfoMat* 4, no. 4 (2022): e12228, https://doi.org/10.1002/inf2.12228.

27. S. Liang, X. Wang, R. Qi, et al., "Bronze-Phase TiO_2 as Anode Materials in Lithium and Sodium-Ion Batteries," *Advanced Functional Materials* 32, no. 25 (2022): 2201675, https://doi.org/10.1002/adfm.202201675.

28. Y. Ma, Y. Ma, G. Giuli, et al., "Introducing Highly Redox-Active Atomic Centers into Insertion-Type Electrodes for Lithium-Ion Batteries," *Advanced Energy Materials* 10, no. 25 (2020): 2000783, https://doi.org/10.1002/aenm.202000783.

29. D. Bresser, B. Oschmann, M. N. Tahir, et al., "Carbon-Coated Anatase TiO_2 Nanotubes for Li- and Na-Ion Anodes," *Journal of the Electrochemical Society* 162, no. 2 (2015): A3013–A3020, https://doi.org/10.1149/2.0031502jes.

30. Y. Ma, Y. Ma, H. Euchner, et al., "An Alternative Charge-Storage Mechanism for High-Performance Sodium-Ion and Potassium-Ion Anodes," *ACS Energy Letters* 6, no. 3 (2021): 915–924, https://doi.org/10.1021/acsenergylett.0c02365.

31. B. Zhao, G. Suo, R. Mu, et al., "Confining WS_2 Hierarchical Structures Into Carbon Core-Shells for Enhanced Sodium Storage," *Journal of Colloid and Interface Science* 677 (2025): 637–646, https://doi.org/10.1016/j.jcis.2024.08.115.

32. F. Lin, I. Alxneit, and A. Wokaun, "Structural and Chemical Changes of Zn-Doped CeO_2 Nanocrystals Upon Annealing at Ultra-High Temperatures," *CrystEngComm* 17, no. 7 (2015): 1646–1653, https://doi.org/10.1039/C4CE02202E.

33. C. I. Hiley, H. Y. Playford, J. M. Fisher, et al., "Pair Distribution Function Analysis of Structural Disorder by Nb^{5+} Inclusion in Ceria: Evidence for Enhanced Oxygen Storage Capacity From Under-Coordinated Oxide," *Journal of the American Chemical Society* 140, no. 5 (2018): 1588–1591, https://doi.org/10.1021/jacs.7b12421.

34. O. A. Marina, C. Bagger, S. Primdahl, and M. Mogensen, "A Solid Oxide Fuel Cell With a Gadolinia-Doped Ceria Anode: Preparation and Performance," *Solid State Ionics* 123, no. 1–4 (1999): 199–208, https://doi.org/10.1016/S0167-2738(99)00111-3.

35. S. Ning, Z. Guo, J. Wang, S. Huang, S. Chen, and X. Kang, "Sn-Doped CeO_2 Nanorods as High-Performance Electrocatalysts for CO_2 Reduction to Formate," *Chemelectrochem* 8, no. 14 (2021): 2680–2685, https://doi.org/10.1002/celc.202100445.

36. F. d'Acapito, G. O. Lepore, A. Puri, et al., "The LISA Beamline at ESRF," *Journal of Synchrotron Radiation* 26, no. 2 (2019): 551–558, https://doi.org/10.1107/S160057751801843X.

37. P. A. Lee, P. H. Citrin, P. Eisenberger, and B. M. Kincaid, "Extended X-Ray Absorption Fine Structure—Its Strengths and Limitations as a Structural Tool," *Reviews of Modern Physics* 53, no. 4 (1981): 769–806, https://doi.org/10.1103/RevModPhys.53.769.

38. B. Ravel and M. Newville, "ATHENA, ARTEMIS, HEPHAESTUS: Data Analysis for X-Ray Absorption Spectroscopy Using IFEFFIT," *Journal of Synchrotron Radiation* 12, no. 4 (2005): 537–541, https://doi.org/10.1107/S0909049505012719.

39. B. Ravel, "ATOMS: Crystallography for the X-Ray Absorption Spectroscopist," *Journal of Synchrotron Radiation* 8, no. 2 (2001): 314–316, https://doi.org/10.1107/S090904950001493X.

40. C. S. Barrett, P. Cucka, and K. Haefner, "The Crystal Structure of Antimony at 4.2, 78 and 298 K," *Acta Crystallographica* 16, no. 6 (1963): 451–453, https://doi.org/10.1107/S0365110X63001262.

41. M. Jansen, "Crystal Structure of Sb_2O_5," *Angewandte Chemie International Edition* 17, no. 2 (1978): 137–138, https://doi.org/10.1002/anie.197801371.

42. G. Brauer and H. Gradinger, "Über Heterotype Mischphasen bei Seltenerdoxyden. II. Die Oxydsysteme des Cers und des Praseodyms," *Zeitschrift für Anorganische und Allgemeine Chemie* 277, no. 1–2 (1954): 89–95, https://doi.org/10.1002/zaac.19542770110.

43. A. L. Ankudinov, B. Ravel, J. J. Rehr, and S. D. Conradson, "Real-Space Multiple-Scattering Calculation and Interpretation of X-Ray-Absorption Near-Edge Structure," *Physical Review B* 58, no. 12 (1998): 7565–7576, https://doi.org/10.1103/PhysRevB.58.7565.

44. G. O. Lepore, Y. Li, and X. Xue, *Elucidating the Lithium Storage Mechanism of Ruthenium-Doped Cerium Oxide Anodes via Ex Situ & Operando X-Ray Absorption Spectroscopy* (European Synchrotron Radiation Facility, 2026).

45. S. Nannarone, F. Borgatti, A. DeLuisa, et al., "The BEAR Beamline at Elettra," *AIP Conference Proceedings* 705 (2004): 450–453, https://doi.org/10.1063/1.1757831.

46. D. Bresser, E. Paillard, R. Kloepsch, et al., "Carbon-Coated $ZnFe_2O_4$ Nanoparticles for Advanced Lithium-Ion Anodes," *Advanced Energy Materials* 3, no. 4 (2013): 513–523, https://doi.org/10.1002/aenm.201200735.

47. X. Dong, X. Liu, H. Li, S. Passerini, and D. Bresser, "Single-Ion Conducting Polymer Electrolyte for Superior Sodium-Metal Batteries," *Angewandte Chemie International Edition* 62, no. 43 (2023): e202308699, https://doi.org/10.1002/anie.202308699.

48. B. A. Boukamp, "A Nonlinear Least Squares Fit Procedure for Analysis of Immittance Data of Electrochemical Systems," *Solid State Ionics* 20, no. 1 (1986): 31–44, https://doi.org/10.1016/0167-2738(86)90031-7.

49. B. A. Boukamp, "A Package for Impedance/Admittance Data Analysis," *Solid State Ionics* 18–19 (1986): 136–140, https://doi.org/10.1016/0167-2738(86)90100-1.

50. G. Kresse and J. Furthmüller, "Efficient Iterative Schemes for Ab Initio Total-Energy Calculations Using a Plane-Wave Basis Set," *Physical Review B* 54, no. 16 (1996): 11169–11186, https://doi.org/10.1103/PhysRevB.54.11169.

51. G. Kresse and D. Joubert, "From Ultrasoft Pseudopotentials to the Projector Augmented-Wave Method," *Physical Review B* 59, no. 3 (1999): 1758–1775, https://doi.org/10.1103/PhysRevB.59.1758.

52. J. P. Perdew, K. Burke, and M. Ernzerhof, "Generalized Gradient Approximation Made Simple," *Physical Review Letters* 77, no. 18 (1996): 3865–3868, https://doi.org/10.1103/PhysRevLett.77.3865.

53. M. Deng, S. Li, W. Hong, et al., "Octahedral Sb_2O_3 as High-Performance Anode for Lithium and Sodium Storage," *Materials Chemistry and Physics* 223 (2019): 46–52, https://doi.org/10.1016/j.matchemphys.2018.10.043.

54. J. Li, L. Han, X. Zhang, et al., "Sb_2O_5/Co-Containing Carbon Polyhedra as Anode Material for High-Performance Lithium-Ion Batteries," *Chemical Engineering Journal* 370 (2019): 800–809, https://doi.org/10.1016/j.cej.2019.03.244.

55. D. Schweke, Y. Mordehovitz, M. Halabi, L. Shelly, and S. Hayun, "Defect Chemistry of Oxides for Energy Applications," *Advanced Materials* 30, no. 41 (2018): e1706300, https://doi.org/10.1002/adma.201706300.

56. D. Horlait, L. Claparede, N. Clavier, et al., "Stability and Structural Evolution of $Ce^{IV}_{1-x}Ln^{III}_xO_{2-x/2}$ Solid Solutions: A Coupled μ-Raman/XRD Approach," *Inorganic Chemistry* 50, no. 15 (2011): 7150–7161, https://doi.org/10.1021/ic200751m.

57. C. I. Hiley, J. M. Fisher, R. J. Kashtiban, G. Cibin, D. Thompsett, and R. I. Walton, "Incorporation of Sb^{5+} Into CeO_2: Local Structural Distortion of the Fluorite Structure From a Pentavalent Substituent," *Dalton Transactions* 47, no. 29 (2018): 9693–9700, https://doi.org/10.1039/C8DT01750F.

58. S. Phokha, S. Hunpratub, B. Usher, A. Pimsawat, N. Chanlek, and S. Maensiri, "Effects of CeO_2 Nanoparticles on Electrochemical Properties of Carbon/CeO_2 Composites," *Applied Surface Science* 446 (2018): 36–46, https://doi.org/10.1016/j.apsusc.2018.02.209.

59. M. Kurnatowska, W. Mista, P. Mazur, and L. Kepinski, "Nanocrystalline $Ce_{1-x}Ru_xO_2$ – Microstructure, Stability and Activity in CO and Soot Oxidation," *Applied Catalysis B: Environmental* 148–149 (2014): 123–135, https://doi.org/10.1016/j.apcatb.2013.10.047.

60. C. Yang, X. Yu, S. Heißler, et al., "Surface Faceting and Reconstruction of Ceria Nanoparticles," *Angewandte Chemie International Edition* 56, no. 1 (2017): 375–379, https://doi.org/10.1002/anie.201609179.

61. F. Zhang, P. Wang, J. Koberstein, S. Khalid, and S. W. Chan, "Cerium Oxidation State in Ceria Nanoparticles Studied With X-Ray Photoelectron Spectroscopy and Absorption Near-Edge Spectroscopy," *Surface Science* 563, no. 1–3 (2004): 74–82, https://doi.org/10.1016/j.susc.2004.05.138.

62. Y. Ding, L. Huang, J. Zhang, et al., "Ru-Doped, Oxygen-Vacancy-Containing CeO_2 Nanorods Toward N_2 Electroreduction," *Journal of Materials Chemistry A* 8, no. 15 (2020): 7229–7234, https://doi.org/10.1039/D0TA02211J.

63. C. Barth, C. Laffon, R. Olbrich, A. Ranguis, P. Parent, and M. Reichling, "A Perfectly Stoichiometric and Flat CeO_2(111) Surface on a Bulk-Like Ceria Film," *Scientific Reports* 6, no. 1 (2016): 21165, https://doi.org/10.1038/srep21165.

64. S. Neupane, D. Mishra, K. B. Nakarmi, D. K. Gupta, R. J. Yadav, and A. P. Yadav, "Preparation of Antimony Oxide in Different Media and Its Effect on the pH Measurement," *Analytical and Bioanalytical Electrochemistry* 13 (2021): 127–138, ISSN: 20084226.

65. O. C. Gagné and F. C. Hawthorne, "Comprehensive Derivation of Bond-Valence Parameters for Ion Pairs Involving Oxygen," *Acta Crystallographica Section B: Structural Science, Crystal Engineering and Materials* 71, no. 5 (2015): 562–578, https://doi.org/10.1107/S2052520615016297.

66. P. Makula, M. Pacia, and W. Macyk, "How to Correctly Determine the Band Gap Energy of Modified Semiconductor Photocatalysts Based on UV-Vis Spectra," *Journal of Physical Chemistry Letters* 9, no. 23 (2018): 6814–6817, https://doi.org/10.1021/acs.jpclett.8b02892.

67. T. Kolodiazhnyi, T. Charoonsuk, M. Spreitzer, and N. Vittayakorn, "Analysis of Sb-Doped Ceria: Magnetism, Conductivity, Dielectric, Specific Heat and Optical Properties," *Journal of the European Ceramic Society* 39, no. 2–3 (2019): 418–423, https://doi.org/10.1016/j.jeurceramsoc.2018.09.009.

68. C. Hua, X. Fang, Z. Yang, Y. Gao, Z. Wang, and L. Chen, "Lithium Storage Mechanism and Catalytic Behavior of CeO_2," *Electrochemistry Communications* 25 (2012): 66–69, https://doi.org/10.1016/j.elecom.2012.09.030.

69. C. M. Park, S. Yoon, S. Lee, J. H. Kim, J. H. Jung, and H. J. Sohn, "High-Rate Capability and Enhanced Cyclability of Antimony-Based Composites for Lithium Rechargeable Batteries," *Journal of the Electrochemical Society* 154, no. 10 (2007): A917–A920, https://doi.org/10.1149/1.2761829.

70. E. Barcaro, V. Marangon, M. Mutarelli, and J. Hassoun, "A Lithium-Ion Battery With Cycling Stability Promoted by the Progressive Activation of a Silicon Oxide Anode in Graphene-Amorphous Carbon Matrix," *Journal of Power Sources* 595 (2024): 234059, https://doi.org/10.1016/j.jpowsour.2024.234059.

71. K. Li, X. Zhou, A. Nie, et al., "Discovering a First-Order Phase Transition in the Li–CeO_2 System," *Nano Letters* 17, no. 2 (2017): 1282–1288, https://doi.org/10.1021/acs.nanolett.6b05126.

72. J. Qian, Y. Chen, L. Wu, Y. Cao, X. Ai, and H. Yang, "High Capacity Na-Storage and Superior Cyclability of Nanocomposite Sb/C Anode for Na-Ion Batteries," *Chemical Communications* 48, no. 56 (2012): 7070–7072, https://doi.org/10.1039/C2CC32730A.

73. V. Marangon, E. Barcaro, F. De Boni, M. Prato, D. Bresser, and J. Hassoun, "Effective Liquid Electrolytes for Enabling Room-Temperature Sodium–Sulfur Batteries," *Advanced Sustainable Systems* 8, no. 11 (2024): 2400268, https://doi.org/10.1002/adsu.202400268.

74. X. Yi, X. Li, J. Zhong, et al., "Unraveling the Mechanism of Different Kinetics Performance Between Ether and Carbonate Ester Electrolytes in Hard Carbon Electrode," *Advanced Functional Materials* 32, no. 48 (2022): 2209523, https://doi.org/10.1002/adfm.202209523.

75. Z. Lin, Q. Xia, W. Wang, W. Li, and S. Chou, "Recent Research Progresses in Ether- and Ester-Based Electrolytes for Sodium-Ion Batteries," *InfoMat* 1, no. 3 (2019): 376–389, https://doi.org/10.1002/inf2.12023.

76. L. Habib, G. Suo, C. Lin, et al., "Strategies in Improving the Initial Coulombic Efficiency of Transition Metal Chalcogenides Anode Materials for Sodium-Ion Batteries: A Review," *Renewable and Sustainable Energy Reviews* 217 (2025): 115721, https://doi.org/10.1016/j.rser.2025.115721.

77. G. A. Muller, J. B. Cook, H. S. Kim, S. H. Tolbert, and B. Dunn, "High Performance Pseudocapacitor Based on 2D Layered Metal Chalcogenide Nanocrystals," *Nano Letters* 15, no. 3 (2015): 1911–1917, https://doi.org/10.1021/nl504764m.

78. J. Wang, J. Polleux, J. Lim, and B. Dunn, "Pseudocapacitive Contributions to Electrochemical Energy Storage in TiO_2 (Anatase) Nanoparticles," *Journal of Physical Chemistry C* 111, no. 40 (2007): 14925–14931, https://doi.org/10.1021/jp074464w.

79. S. J. Rezvani, R. Gunnella, A. Witkowska, et al., "Is the Solid Electrolyte Interphase an Extra-Charge Reservoir in Li-Ion Batteries?," *ACS Applied Materials & Interfaces* 9, no. 5 (2017): 4570–4576, https://doi.org/10.1021/acsami.6b12408.

80. M. N. Revoy, R. W. J. Scott, and A. P. Grosvenor, "Ceria Nanocubes: Dependence of the Electronic Structure on Synthetic and Experimental Conditions," *Journal of Physical Chemistry C* 117, no. 19 (2013): 10095–10105, https://doi.org/10.1021/jp3124814.

81. E. Paparazzo, "XPS Studies of Damage Induced by X-Ray Irradiation on CeO_2 Surfaces," *Surface Science* 234, no. 1–2 (1990): L253–L258, https://doi.org/10.1016/0039-6028(90)90658-U.

82. L. Zhang, X. Li, A. Augustsson, et al., "Revealing the Electronic Structure of LiC_6 by Soft X-Ray Spectroscopy," *Applied Physics Letters* 110, no. 10 (2017): 104106, https://doi.org/10.1063/1.4978432.

83. C. Yogi, D. Takamatsu, K. Yamanaka, et al., "Soft X-Ray Absorption Spectroscopic Studies With Different Probing Depths: Effect of an Electrolyte Additive on Electrode Surfaces," *Journal of Power Sources* 248 (2014): 994–999, https://doi.org/10.1016/j.jpowsour.2013.10.030.

84. A. Augustsson, M. Herstedt, J. H. Guo, et al., "Solid Electrolyte Interphase on Graphite Li-Ion Battery Anodes Studied by Soft X-Ray Spectroscopy," *Physical Chemistry Chemical Physics* 6, no. 16 (2004): 4185–4189, https://doi.org/10.1039/B313434B.

85. Y. Kim, D. S. Kim, J. H. Um, J. Yoon, H. Kim, and W.-S. Yoon, "Revisiting Solid Electrolyte Interphase on the Carbonaceous Electrodes Using Soft X-Ray Absorption Spectroscopy," *ACS Applied Materials & Interfaces* 10, no. 35 (2018): 29992–29999, https://doi.org/10.1021/acsami.8b09939.

86. Y. Wang, X. Wang, B. Zhao, et al., "Molecular-Level Identification of Organic Species of Ether-Based Solid-Electrolyte Interphase in Sodium-Ion Batteries," *Nano Energy* 120 (2024): 109163, https://doi.org/10.1016/j.nanoen.2023.109163.

87. J. Tsuji, H. Nakamatsu, T. Mukoyama, K. Kojima, S. Ikeda, and K. Taniguchi, "Lithium K-Edge XANES Spectra for Lithium Compounds," *X-Ray Spectrometry* 31, no. 4 (2002): 319–326, https://doi.org/10.1002/xrs.577.

88. S. J. Rezvani, F. Nobili, R. Gunnella, et al., "SEI Dynamics in Metal Oxide Conversion Electrodes of Li-Ion Batteries," *Journal of Physical Chemistry C* 121, no. 47 (2017): 26379–26388, https://doi.org/10.1021/acs.jpcc.7b08259.

89. I. Moeez, D. Susanto, W. Chang, H. D. Lim, and K. Y. Chung, "Artificial Cathode Electrolyte Interphase by Functional Additives Toward Long-Life Sodium-Ion Batteries," *Chemical Engineering Journal* 425 (2021): 130547, https://doi.org/10.1016/j.cej.2021.130547.

90. T. Eisenmann, J. Asenbauer, S. J. Rezvani, et al., "Impact of the Transition Metal Dopant in Zinc Oxide Lithium-Ion Anodes on the Solid

Electrolyte Interphase Formation," *Small Methods* 5, no. 4 (2021): e2001021, https://doi.org/10.1002/smtd.202001021.

91. J. E. N. Swallow, M. W. Fraser, N. J. H. Kneusels, et al., "Revealing Solid Electrolyte Interphase Formation Through Interface-Sensitive Operando X-Ray Absorption Spectroscopy," *Nature Communications* 13, no. 1 (2022): 6070, https://doi.org/10.1038/s41467-022-33691-1.

92. K. Y. Chung, W. S. Yoon, K. B. Kim, B. W. Cho, and X. Q. Yang, "Formation of an SEI on a $LiMn_2O_4$ Cathode During Room Temperature Charge–Discharge Cycling Studied by Soft X-Ray Absorption Spectroscopy at the Fluorine K-Edge," *Journal of Applied Electrochemistry* 41, no. 11 (2011): 1295–1299, https://doi.org/10.1007/s10800-011-0344-6.

93. W. Zaheer, J. L. Andrews, A. Parija, et al., "Reversible Room-Temperature Fluoride-Ion Insertion in a Tunnel-Structured Transition Metal Oxide Host," *ACS Energy Letters* 5, no. 8 (2020): 2520–2526, https://doi.org/10.1021/acsenergylett.0c01328.

94. L. B. Darwiche, L. Madec, L. Monconduit, and H. Martinez, "Impact of the Salts and Solvents on the SEI Formation in Sb/Na Batteries: An XPS Analysis," *Electrochimica Acta* 207 (2016): 284–292, https://doi.org/10.1016/j.electacta.2016.03.089.

95. K. Li, J. Zhang, D. Lin, et al., "Evolution of the Electrochemical Interface in Sodium Ion Batteries With Ether Electrolytes," *Nature Communications* 10, no. 1 (2019): 725, https://doi.org/10.1038/s41467-019-08506-5.

Supporting Information

Additional supporting information can be found online in the Supporting Information section.
Supporting Information S1: rar270384-sup-0001-suppl-data.docx.